BEILSTEIN JOURNAL OF NANOTECHNOLOGY

Smart nanomaterials in electronics and photonics

Edited by Yogendra Kumar Mishra, Rosaria Puglisi, Dawid Janas and Teresa Monteiro

Imprint

Beilstein Journal of Nanotechnology
www.bjnano.org
ISSN 2190-4286
Email: journals-support@beilstein-institut.de

The *Beilstein Journal of Nanotechnology* is published by the Beilstein-Institut zur Förderung der Chemischen Wissenschaften.

Beilstein-Institut zur Förderung der Chemischen Wissenschaften
Trakehner Straße 7–9
60487 Frankfurt am Main
Germany
www.beilstein-institut.de

BEILSTEIN JOURNAL OF NANOTECHNOLOGY

Investigating ripple pattern formation and damage profiles in Si and Ge induced by 100 keV Ar^+ ion beam: a comparative study

Indra Sulania[*1,2], Harpreet Sondhi[3,4], Tanuj Kumar[5], Sunil Ojha[1], G R Umapathy[1], Ambuj Mishra[1], Ambuj Tripathi[1], Richa Krishna[3], Devesh Kumar Avasthi[6] and Yogendra Kumar Mishra[2]

Full Research Paper

Open Access

Address:
[1]Inter University Accelerator Centre, Aruna Asaf Ali Marg, New Delhi 110067, India, [2]SmartMaterials, Mads Clausen Institute, University of Southern Denmark, Alison 2 6400, Denmark, [3]Amity Institute of Nanotechnolgy, Amity University, Noida 201303, India, [4]Katholieke University, Faculty of Engineering Science, Leuven 3000, Belgium, [5]Department of Nanoscience and Materials, Central University of Jammu, Jammu 181143, India and [6]Centre for Interdisciplinary Research and Innovation, University of Petroleum and Energy Studies University, Dehradun 248007, India

Email:
Indra Sulania[*] - indra.sulaniya@gmail.com

* Corresponding author

Keywords:
atomic force microscopy; ion beam; nanopatterns; radiation damage; Rutherford backscattering spectrometry; transmission electron microscopy

Beilstein J. Nanotechnol. **2024,** *15,* 367–375.
https://doi.org/10.3762/bjnano.15.33

Received: 26 November 2023
Accepted: 12 March 2024
Published: 05 April 2024

This article is part of the thematic issue "Smart nanomaterials in electronics and photonics".

Associate Editor: S. A. Claridge

Abstract

Desired modifications of surfaces at the nanoscale may be achieved using energetic ion beams. In the present work, a complete study of self-assembled ripple pattern fabrication on Si and Ge by 100 keV Ar^+ ion beam bombardment is discussed. The irradiation was performed in the ion fluence range of ≈3×10^{17} to 9×10^{17} ions/cm^2 and at an incident angle of $\theta \approx 60°$ with respect to the surface normal. The investigation focuses on topographical studies of pattern formation using atomic force microscopy, and induced damage profiles inside Si and Ge by Rutherford backscattering spectrometry and transmission electron microscopy. The ripple wavelength was found to scale with ion fluence, and energetic ions created more defects inside Si as compared to that of Ge. Although earlier reports suggested that Ge is resistant to structural changes upon Ar^+ ion irradiation, in the present case, a ripple pattern is observed on both Si and Ge. The irradiated Si and Ge targets clearly show visible damage peaks between channel numbers (1000–1100) for Si and (1500–1600) for Ge. The clustering of defects leads to a subsequent increase of the damage peak in irradiated samples (for an ion fluence of ≈9×10^{17} ions/cm^2) compared to that in unirradiated samples.

Introduction

Scientific research varying from electronics to photonics, homeland security, high-resolution parallel patterning of magnetic media, biotechnology, and medicine are based upon nanotechnology. These applications require nanopatterning techniques to fabricate devices or structures. Although these structures may not be visible to the naked eye, they certainly have a visible impact on the mentioned applications. Nanopatterning is a very delicate procedure that is only possible with special techniques such as ion beam sputtering (IBS), with which one can achieve nanostructures in a controlled manner on a wide variety of substrates with required dimensions. There are reports from 1960's, by Cunningham et al. [1] and Navez et al. [2], on the production of submicron and nanoscale patterns by IBS. However, with the availability of high-resolution tools such as atomic force microscopy (AFM) [3] and transmission electron microscopy (TEM), it is possible to visualize these features. Formation of dots, ripples, and pits have been well studied using IBS [4-9]. In the last few decades, numerous efforts have been made to understand IBS through simulations [10] as well as experimental results [11,12]. Thanks to these efforts, desired nanopattern features with a large degree of control may be achieved, according to specific applications, on a wide variety of targets. Facsko et al. [13] have shown controlled growth of nanodots on GaSb, and their probable use was demonstrated via photoluminescence spectroscopy. Stupp et al. [14] have explored possible applications of self-assembly of biomolecules with controlled stereochemistry in materials technology. However, the fundamental reasoning behind how this self-organization process evolves in terms of defect creation or damage still needs to be understood.

Despite controlled fabrication of patterns has been achieved, details that influence the process of self-assembly still remain open. Ion beam sputtering is an important method for inducing topographical changes in specific materials. For silicon, self-organized dots, ripples, and cones have been observed [15], which may be achieved by altering the ion incidence angle [16]. However, there are some inconsistencies and replicability issues between the studies, which might mean that other experimental parameters might be important for the formation of these nanostructures. Computational studies have provided relevance and connections between experiments and theoretical modelling [4,17-24]. Basic models to explain IBS were initially given by Thompson et al. [25] and Sigmund et al. [26], based on the radiation damage in bulk materials. When an energetic ion strikes a target surface, it may lose its energy in the following ways. If the ion has enough energy to cross the repulsive potential energy barrier of target atoms at the surface, it will pass through the solid. A collision cascade is created within the target atoms during the slowing-down course. The impinging ion subsequently transfers its energy to the atoms of the target material in all the collisions and finally stops. When this energy transfer is sufficient, a displacement of atoms from their equilibrium positions creating a vacancy or a recoil occurs. Alternatively, if the ion energy is high enough such recoils may create additional displacement of atoms through a cascade effect with subsequent decrement in their energy. In due course, the recoil energies are quenched in short timescales of $\approx 10^{-15}$ seconds. The modified target volume, which gets affected due to this slowing down process, depends on the mass and energy of the incoming ion and on the mass of the target atom. It may be expressed as the spatial distribution of the energy transferred/deposited within the target [27,28]. Sometimes the energy distribution on the target atoms at the surface may be sufficient to overcome binding energies so as to knock them out of the surfaces through an outwardly directed momentum. This process is known as sputtering [26], and the number of ejected atoms per ion is given by the sputtering yield, $Y(\theta)$. It is clearly visible that Y is a function of the incident angle θ, and it maximizes around $\theta \approx 60°$. Ion–matter interaction in low-energy regimes is well understood; however, a few empirical additions have been taking place in the formulism based upon the experimental observations [29,30]. A large group of theoreticians have contributed to the already existing classic description given by Bradley and Harper [31] based on morphological effects of IBS. The height $h(x, y, t)$ of the sputtered surface can be described by a linear equation (Equation 1):

$$\frac{\partial h}{\partial t} = -\nu_0 + \Upsilon\nabla h + \nu\nabla^2 h - D\nabla^4 h \qquad (1)$$

where ν_0 is the constant erosion velocity, ν is the effective surface tension, and D denotes the surface diffusion which is activated by different physical processes (i.e., thermal diffusion and ion-induced diffusion) [32]. This approach is based on the linear cascade model and Gaussian approximation of energy distribution as developed by Sigmund [26] to describe ion–atom collisions inside the target.

Rutherford backscattering spectrometry (RBS) studies in the channelling mode have been used to study defects in crystals for more than a few decades now [33,34]. It imparts the useful information about the structure and composition of materials through the damage fraction studies of ion-bombarded crystalline samples by detecting the backscattered beam of high-energy ions ($He^+ \approx 1$–2 MeV). It impinges on the target material which provides good mass and depth resolution and also probes smaller radiation damages [35]. The damage produced by ion implantation in semiconductors consists of randomly distributed atoms displaced from their regular lattice sites up to a

depth or range of damage profiles. Single-crystal materials (e.g. silicon and germanium) are composed of ordered arrays of atoms. If an ion beam is aligned to the atomic planes, most of the ions pass through the interplanar space and penetrate deep into the crystal. This can be used in channelling studies to analyse the crystal structure and to locate interstitial atoms within the array of target atoms. The relation between yield and defect concentration was derived by Bøgh [33]. It provides information about the depth distribution of defects in the first few microns beneath the crystalline surface. Channelling is an important process which has been heavily studied by Norlund et al. [24] and Hobler et al. [36]. Thus, in our studies, RBS-c plays a significant role in understanding the damage fractions in Si and Ge due to Ar^+ ions. In the present work, 100 keV Ar^+ ion bombardment was simultaneously performed on Si and Ge substrates. A correlation between ripple morphology and ion beam parameters was derived to understand the damage incurred by Ar^+ ions inside both materials using RBS-c measurements.

Experimental Details

Commercially available Si and Ge wafers, procured from Semiconductor wafers Inc., were taken and cut into equal pieces of 0.5 cm × 1 cm. The samples were mounted on an experimental ladder used for irradiation experiments using double-sided tape. Pieces of Si were mounted on the left-hand side and of Ge on the right-hand side of the Cu ladder. This was done to allow them to be simultaneously irradiated, keeping the experimental conditions the same. The experiment was performed at high vacuum ≈5×10^{-6} Torr and at room temperature. Argon ions (100 keV) have been used to irradiate the samples at an incident angle of θ ≈ 60° with respect to the surface normal [16]. The area in which the ion beam fell was kept larger (1 × 1) cm^2 to allow for the simultaneous irradiation of both samples (Si and Ge). The time was calculated using Equation 2:

$$T(\text{sec}) = (\phi \times A) \Big/ \left(I \times 6.25 \times 10^9\right), \qquad (2)$$

where ϕ is the ion fluence in ions/cm^2, A is the area of the sample in cm^2, and I is the current in particle per nanoampere.

The ion fluence was chosen from the literature [37,38] as 3, 5, 7, and 9×10^{17} ions/cm^2 to induce complete amorphization within the two surfaces up to the ion range. The ion irradiation experiment was performed in the 90-degree beam line dedicated for materials science experiments in the Low-Energy Ion Beam (LEIB) facility of the Inter University Accelerator Centre, New Delhi. The electronic and nuclear energy losses of 100 keV Ar^+ inside Si and Ge were calculated using the SRIM software [39]. The electronic energy loss values were found to be 37.67 and 36.51 eV/Å for Si and Ge, respectively, and the nuclear energy loss values were found to be 47.75 and 59.61 eV/Å for Si and Ge, respectively. The range of Ar ions in Si is 106.5 nm and that in Ge is 72.2 nm. The pristine and irradiated samples were characterized by AFM (Nanoscope IIIa controller, Bruker, USA) using an RTESP tip with radius of curvature of ≈10 nm. The RBS measurements were performed in channelling mode using 2 MeV He^+ ions at the PARAS facility at the Inter University Accelerator Centre (IUAC), New Delhi, and transmission electron microscopy (TEM) using an equipment from Jeol, Japan. The samples for TEM were prepared for cross-sectional studies in the TEM sample preparation lab at IUAC, New Delhi.

Results and Discussion

Atomic force microscopy studies

Energetic ions, of a few hundreds of kiloelectronvolts, from the ion implanters modify the surface of the target material to grow nanopatterns. The surfaces of the pristine and ion-treated samples were studied via AFM for the surface topography and change in root-mean-square (RMS) surface roughness. Figure 1 shows AFM images of pristine and 100 keV Ar^+ ion-irradiated Si samples. Pristine samples show a smooth surface with a surface roughness of ≈0.5 nm as observed in Figure 1A (a).

Figure 1A (b–e) shows the surface topography of the irradiated samples at respective ion fluences of (b) 3×10^{17}, (c) 5×10^{17}, (d) 7×10^{17}, and (e) 9×10^{17} ions/cm^2. The surface roughness (R_q) is found to be increased with ion fluence from ≈1.0 nm to 1.6 nm due to ion-induced sputtering at a 60° incidence angle. The pattern formation starts on any surface with amorphization through ion-induced defects resulting from collision cascades [16]. As shown in the AFM micrographs, the Si surface shows ripple patterns. These ripples are more organized and become more regular with ion fluence, with a ripple wavelength ranging from 400 to 740 nm (Figure 1B). The ripple patterns are more pronounced and have a preferential orientation perpendicular to the ion beam direction (shown by an arrow on each of the AFM images). The wavelength of the ripples obtained for initial fluences was ≈430 nm, and became wider (≈740 nm) for an ion fluence of 9×10^{17} ions/cm^2. Figure 2A shows AFM images of pristine and 100 keV Ar^+ ion-irradiated Ge samples. The pristine sample shows a smooth surface with roughness of ≈0.5 nm as observed in Figure 2A (a). Figure 2A (b–e) shows AFM images of irradiated samples at respective ion fluences of (b) 3×10^{17}, (c) 5×10^{17}, (d) 7×10^{17}, and (e) 9×10^{17} ions/cm^2. The Ge surface shows a slight change in the surface roughness to 0.6 nm when irradiated with an ion fluence of 3×10^{17} ions/cm^2. At a fluence of 5×10^{17} ions/cm^2, ripple patterns start appearing on the surface perpendicular to the beam direction (shown by the white arrow in Figure 2) with a roughness of 0.65 nm.

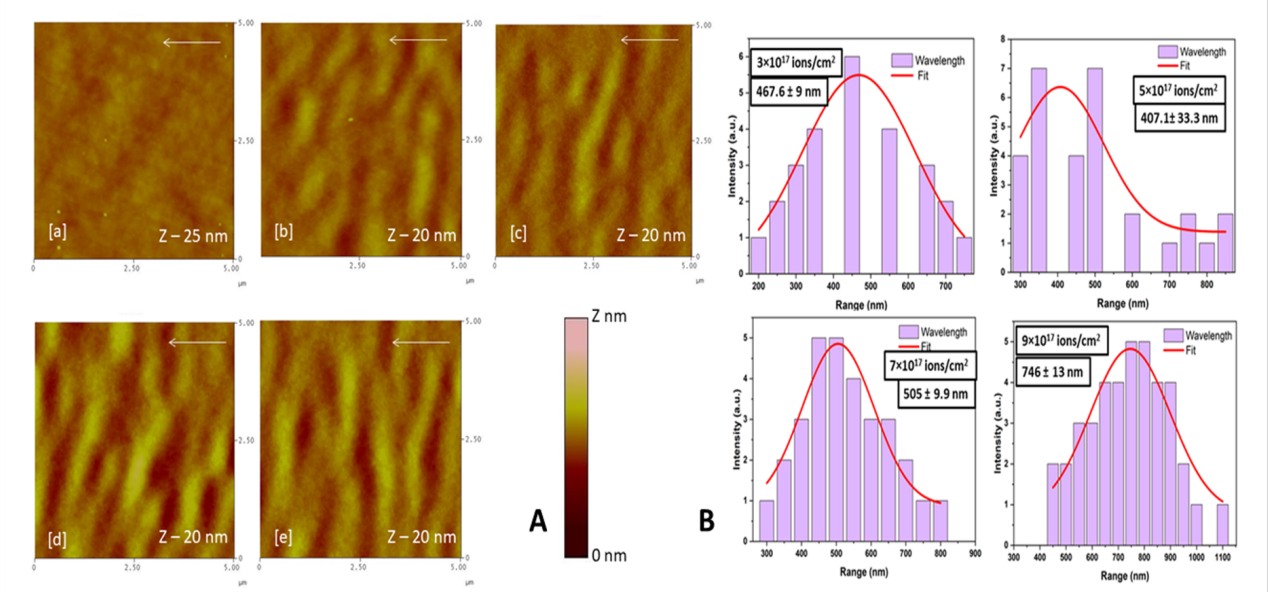

Figure 1: A. AFM images of pristine and 100 keV Ar^+ ion-irradiated Si samples. (a) Pristine and irradiated samples with (b) 3 × 10^{17}, (c) 5 × 10^{17}, (d) 7 × 10^{17}, and (e) 9 × 10^{17} ions/cm^2 (all images are in 5 µm × 5 µm scan size) with corresponding wavelength distribution shown in B.

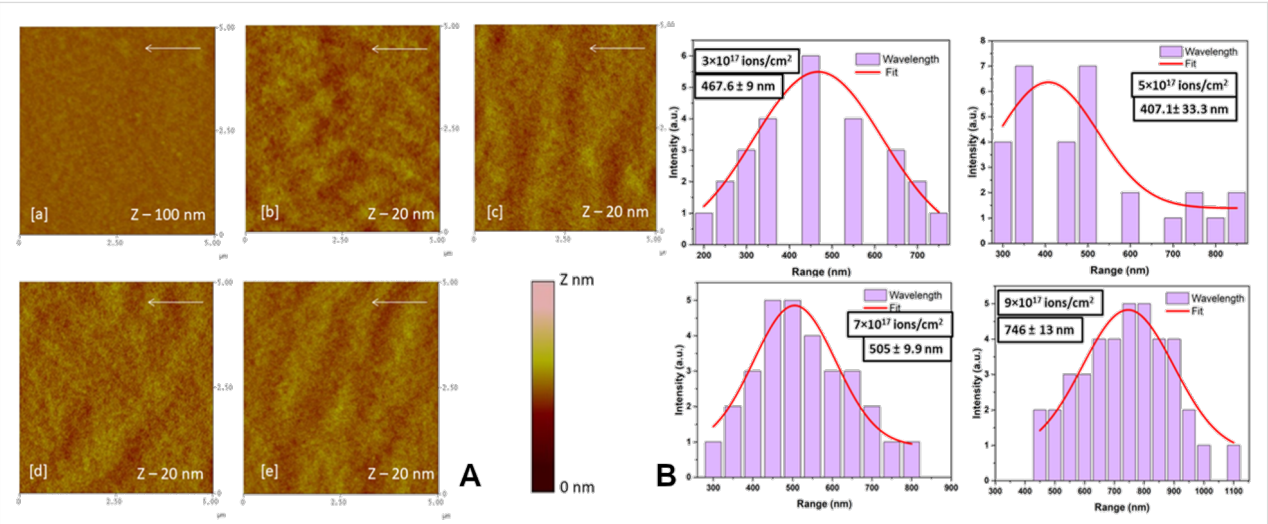

Figure 2: A: AFM images of pristine and 100 keV Ar^+ ion-irradiated Ge samples (a) pristine, (b) 3 × 10^{17}, (c) 5 × 10^{17} (d) 7 × 10^{17} and (e) 9 × 10^{17} ions/cm^2 irradiated samples (all images are in 5 µm × 5 µm scan size), B shows the corresponding wavelength distribution.

The ripples have an average wavelength of ≈370 nm as shown in Figure 2B, with wavelength plots obtained for various ion fluences in the case of Ge samples after irradiation. The wavelength of the ripples obtained for initial fluences was ≈350 nm. The RMS surface roughness of both Si and Ge samples increases with ion fluence. For Si, it changes from 0.5 to 1.2 nm and for Ge it changes from 0.5 to 0.65 nm. It is observed that the patterns formed on Si are more prominent than those on Ge, and this may be due to the choice of Ar^+ ions. It has been shown in the literature that the probability of formation of ripples with Ar^+ ions is higher for Si (m = 28 amu) than that for Ge (m = 72 amu) [9]. This may be due to the mass difference between Si and Ar^+ (m = 40 amu), which is smaller compared to that between Ar^+ and Ge. Therefore, when Ar^+ ions enter the surface of Si, it amorphizes the near surface by inducing defects and irregularity in the Si crystal. On the other hand, since Ge is more massive, it probably requires an ion more massive than Ar or with more energy, ion fluence, or elevated temperature to induce that type of energy deposition in the Ge lattice. This way, the defects can be produced and the substrate can be amorphized. The roughness and growth exponents have been deduced from the RMS surface roughness and power spectral

density data to understand the mechanism of ripple formation on Si and Ge. From the slope, n, of the linear part of power spectral density (PSD) curves, one may find the roughness parameter α using the formula $\alpha = (n - 1)/d$, where d is the dimension of PSD [40]. In our case it is 2. Further, from the log plot of RMS roughness as a function of ion fluence, the slope is obtained as 0.23 ± 0.07 and 0.19 ± 0.09 for Si and Ge, respectively. The roughness parameter α and the growth parameter β give information about the mechanism responsible for creating these surface structures due to the interplay between roughness induced by sputtering and smoothening due to diffusion processes. The values for α and β were found to be α = 0.42 and 0.26 and β = 0.23 and 0.19 for Si and Ge, respectively, indicating that sputtering dominates in both cases to create ripples on the two surfaces. However, this process is better for Si.

Transmission electron microscopy studies

The TEM analysis of Si and Ge samples irradiated with a fluence of 9×10^{17} ions/cm^2 was performed in cross-sectional mode. The TEM image clearly reveals the surface modification occurred due to Ar ion irradiation.

At fewer places, Ar bubbles of ≈15 nm were also visible (marked with a dotted section) in Si. It was found that the samples were still crystalline as seen in Figure 3A and Figure 3B for Si and Ge, respectively with corresponding d-spacing and selected area electron diffraction (SAED) pattern. It was observed that Ge exhibits higher crystallinity as compared to that of Si, even after irradiation at 9×10^{17} ions/cm^2. Due to a higher mass difference between Si and Ge, Ge being a heavier target, there was not too much damage as a result of Ar ion irradiation. Therefore, most of the region remained unaltered beyond the ion penetration depths for both cases. This may be due to the high penetration depth of the electron beam rather than the range of the ion beam. The d-spacing found for Si was 0.31 nm and for Ge was 0.34 nm. The SAED pattern clearly shows a good diffraction pattern for Ge indicating that crystallinity remained intact for Ge even after irradiation at a higher ion fluence than that observed for Si. This further confirms that the near surface region of Si, amorphized to form better ripple patterns in Si as compared to Ge, may be due to the overlap of the collision cascade which led to more defect formation [41].

Rutherford backscattering results

The RBS technique was used to determine the structure and composition of the materials by measuring the backscattering of a beam of high-energy ions (He^+) impinging on a sample. The RBS-channelling spectra of deep ion implants in Si and Ge were analysed to extract the depth profiles of the displaced atoms. Figure 4 shows the aligned spectra for Ge(111) and

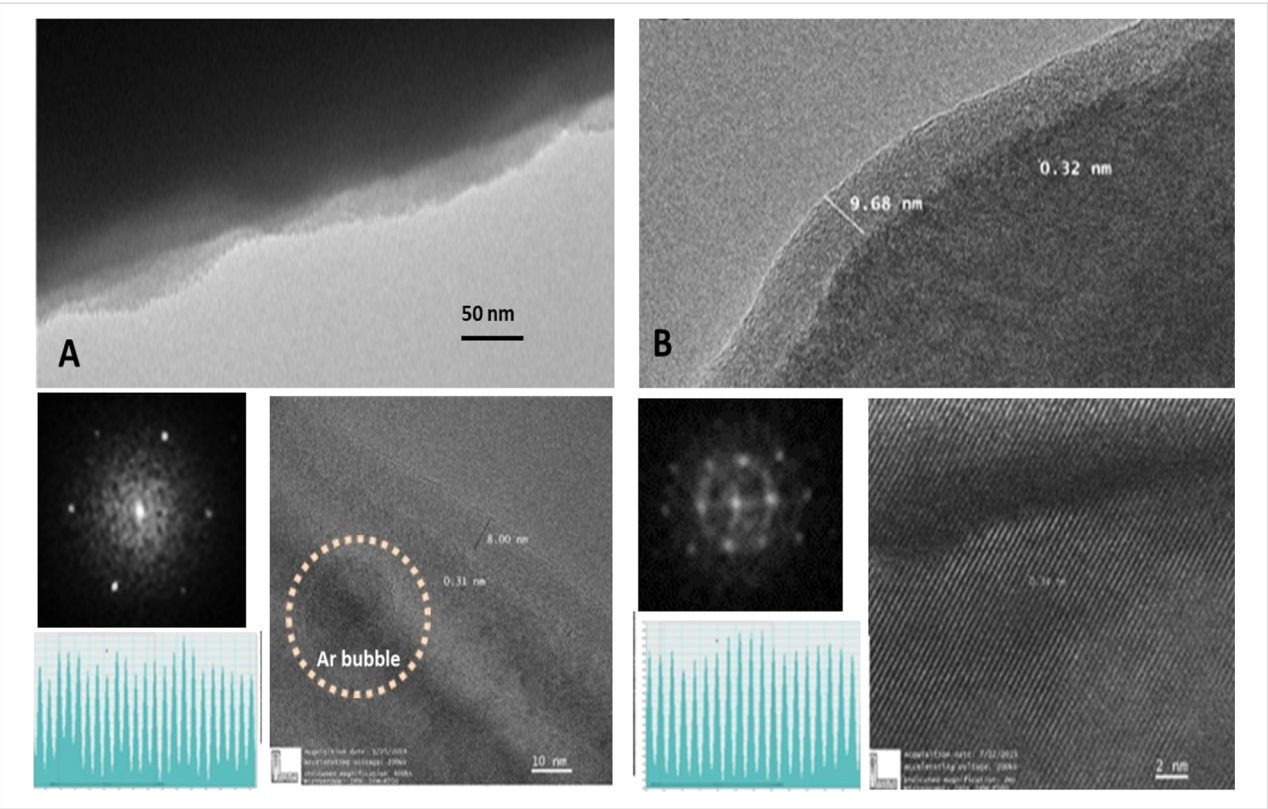

Figure 3: TEM images of A. Si and B. Ge samples irradiated with 9×10^{17} ions/cm^2, with corresponding SAED patterns.

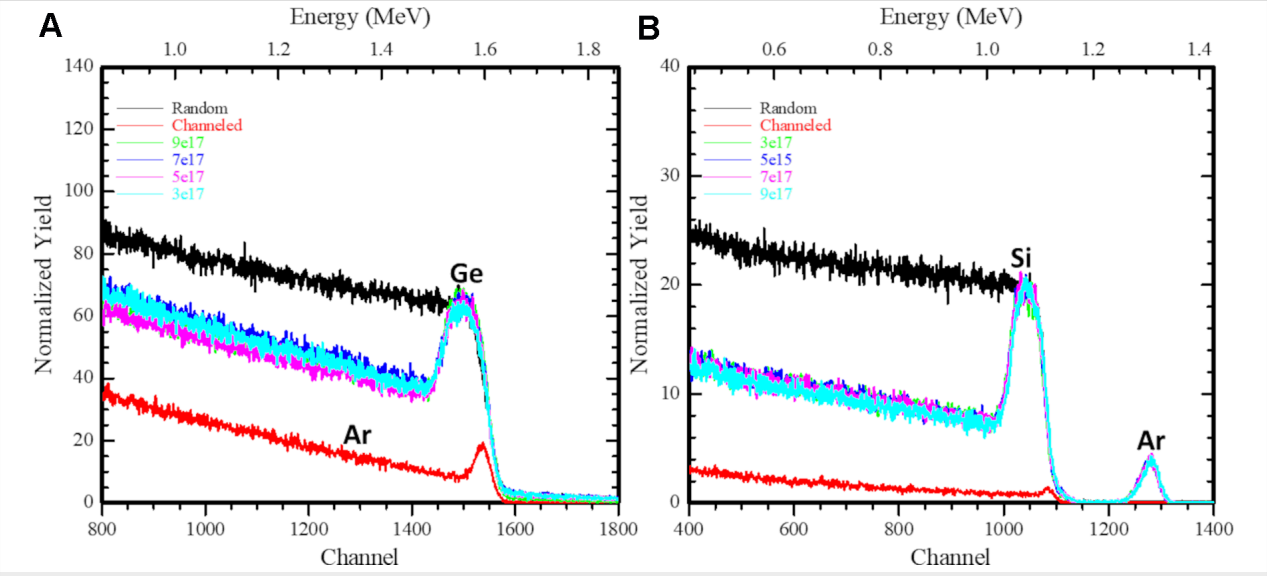

Figure 4: Aligned spectra for (A) Ge and (B) Si targets before and after ion irradiation with 100 keV Ar^+ ions at ion fluences varying from 3 to 9×10^{17} ions/cm^2.

Si(111) targets before and after ion irradiation with 100 keV Ar^+ ions at various ion fluences from 3 to 9×10^{17} ions/cm^2. The crystallinity of the investigated target was determined by the comparison of the aligned spectrum with the random spectra (black). For the pristine Si and Ge samples, the backscattered (BS) yield in an aligned direction reduces to 5% and 7%, respectively. In defect analysis through ion implantation [42], the category-I damage is the subthreshold damage (i.e., partially damaged region) before it completely turns amorphous. On a complete amorphization, an amorphous/crystalline (a/c) interface is formed and further incoming ions create damage beyond this interface or end-range (ER) defects are produced. The irradiated Ge and Si targets clearly show visible damage peaks between channel numbers (1000–1100) for Si and (1500–1600) for Ge. The clustering of defects leads to the subsequent increase of the damage peak in irradiated samples (for an ion fluence of ≈9×10^{17} ions/cm^2) compared to that of unirradiated samples. Typically, an obtained X_{min} value of 4 to 5% indicates good quality of Si and Ge pristine crystals. The increase of de-channelling is attributed to the accumulation of defects produced by Ar irradiation.

The RBS-c spectra recorded for Si and Ge single-crystal samples pre-damaged with 100 keV Ar^+ ions at RT are presented in Figure 5A and Figure 5B, respectively. The RBS spectrum recorded for the pristine sample in random orientation displays two steps corresponding to the backscattering from Si and Ar for channel numbers ≈1050 and ≈1275, respectively. Defect clustering may lead to a subsequent increase of the damage peak in irradiated samples as compared to that of pristine Si and Ge samples. To understand the evolution of the lattice disorder with ion irradiation conditions, the RBS-c data were analyzed and the damage depth distribution (i.e., finite-difference frequency-domain, FDFD, as a function of depth) was extracted by using the simulation code "De-channelling In Crystals And Defect Analysis (DICADA)" [35]. The RBS-c results show Ar in Si spectra, however, due to a lower mass, it is not observed in Ge spectra. The Ar^+ estimated fluence matches the implanted fluence ruling out the possibility of sputtering for Ge. However, Si shows the damage peak around 80 nm with some sputtering of Si atoms. Ar is a period III element, thus, it generates a lower stress field. The depth distribution of defects for pre-damaged crystals before and after Ar^+ irradiation is shown in Figure 5 for Si and Ge. As the Ar^+ fluence is increased, the damage level increases by different amounts towards both the crystal surface up to the depths of 158 nm (A) and 170 nm (B) with an integral density of point defects of ≈0.17×10^{18} per cm^2 and 0.38×10^{17} per cm^2 for Ge and Si, respectively, as calculated by DICADA. This may be due to the tailing effects where an incoming ion comes to rest after travelling a certain distance inside the target material, taking into account the ion straggling.

For Si and Ge, a damage peak is exhibited around ≈75 nm , and the damaged layer extends up to a depth of ≈110 nm, which is consistent with the range of ions calculated with the SRIM code [39,43]. Here, the low-energy part of the spectrum continuously increases, which shows that both samples comprised of in-depth defects even before irradiation, and these defects are high in number in the case of Si (Figure 5C) in comparison to Ge. The area of the damage peak indicates that there are defect accumulations in the irradiated region as shown in Figure 5C,

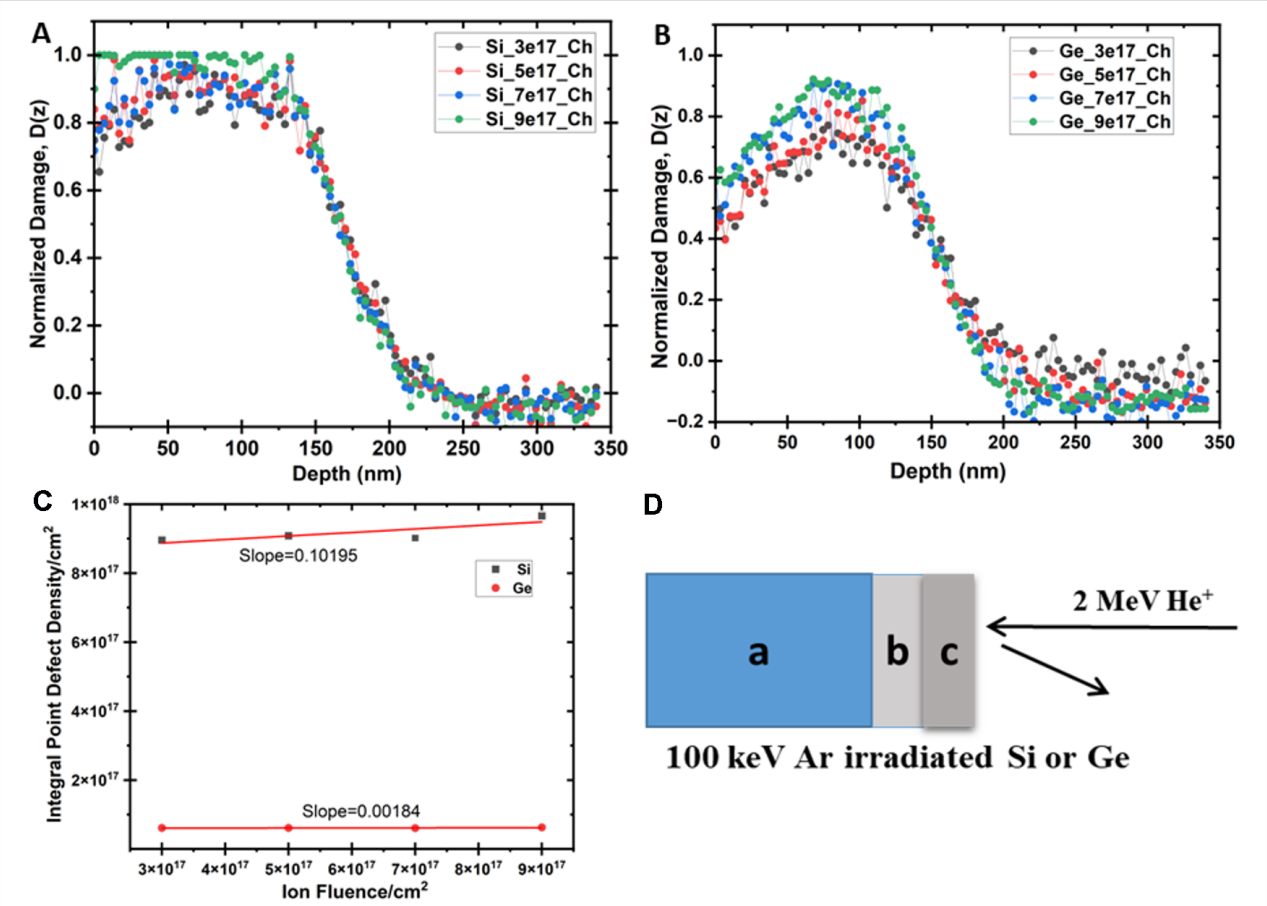

Figure 5: Damage fractions calculated for (A) Si and (B) Ge after irradiation (using the DICADA code. (C) Density of point defects with an increase in ion fluence. (D) Schematic representation of the analysis of amorphous (c) and amorphous/crystalline (b) zones with RBS-c.

which confirms the near surface amorphization in Si in comparison to Ge.

The main defects are the point defects such as interstitials and vacancies produced due to energy transfer between the incoming ions and the target atoms (Figure 6). The range of defect depths calculated from RBS-c spectra for Ar^+ ions irradiated on Ge is 3 to 4% which is lower than that for Si, having 10 to 11% due to differences in mass values of the crystal atoms. However, the damage distribution within the amorphous layer is greater for Ge in comparison with Si implanted samples, and it increases with ion fluence.

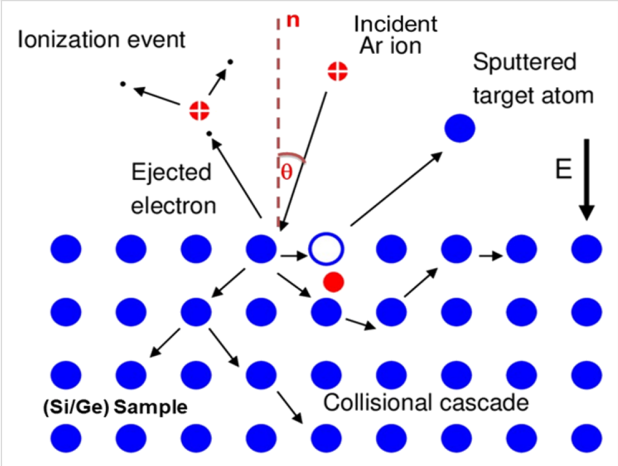

Figure 6: Schematic representation of various defects produced due to low-energy ion interaction with target atoms.

Conclusion

The RBS-c is an effective characterization technique for the estimation of amorphous depth and defect concentration in implanted single crystals. The RBS-c analysis for point defects shows a linear behaviour in defect density with ion fluence. The formation of highly dense dislocation loops beyond the a/c interface results in an increase in the BS yield towards lower channel numbers. The RBS is effective and accurate in determining the sputtering yield for Si and Ge upon incident Ar^+ at 60°. It can be concluded that Ar is creating more defects in Si as compared to that in Ge, resulting in near surface amorphization. Thus, it promotes ripple formation as observed from AFM

images. The ripple wavelength increases with ion fluence in both cases. We observed better ripples in Si in comparison to those in Ge, and the Ge surface shows shallow ripples at fewer spots which were irregular, thus, the ripple formation on Ge is also confirmed.

Supporting Information

Supporting Information File 1

Supplementary files.
[https://www.beilstein-journals.org/bjnano/content/supplementary/2190-4286-15-33-S1.pdf]

Acknowledgements

The authors would like to acknowledge Inter University Accelerator Centre, New Delhi, India, for the beam time and ion beam irradiation facilities.

Funding

IS is grateful for the SIRE fellowship (SIR/2022/001573) awarded to her from SERB, Department of Science and Technology. The authors would like to acknowledge the Department of Science and Technology, India, for funding the SPM facility at IUAC, New Delhi under the Intensification of Research in High Priority Areas (IRHPA) project.

Competing Interests

The authors declare that they have no known competing financial interests or personal relationships that could have appeared to influence the work reported in this paper.

Author Contributions

Indra Sulania: conceptualization; data curation; formal analysis; investigation; methodology; project administration; supervision; validation; writing – original draft; writing – review & editing. Harpreet Sondhi: methodology; software. Tanuj Kumar: resources. Sunil Ojha: data curation; formal analysis. G R Umapathy: formal analysis; software. Ambuj Mishra: data curation. Ambuj Tripathi: data curation. Richa Krishna: data curation. Devesh Kumar Avasthi: resources; supervision. Yogendra Kumar Mishra: funding acquisition; validation.

ORCID® iDs

Indra Sulania - https://orcid.org/0000-0002-4833-1656
Richa Krishna - https://orcid.org/0000-0001-6755-9974

Data Availability Statement

The data that supports the findings of this study is available from the corresponding author upon reasonable request.

References

1. Cunningham, R. L.; Haymann, P.; Lecomte, C.; Moore, W. J.; Trillat, J. J. *J. Appl. Phys.* **1960,** *31,* 839–842. doi:10.1063/1.1735705
2. Navez, M.; Sella, C.; Chaperot, D. *C. R. Hebd. Seances Acad. Sci.* **1962,** *254,* 240–242.
3. Sulania, I.; Yadav, R. P.; Karn, R. K. Atomic and Magnetic Force Studies of Co Thin Films and Nanoparticles: Understanding the Surface Correlation Using Fractal Studies. In *Handbook of Materials Characterization;* Sharma, S. K., Ed.; Springer International Publishing: Cham, Switzerland, 2018; pp 263–291. doi:10.1007/978-3-319-92955-2_7
4. Panchal, V.; Kumar, T.; Sulania, I.; Kumar, S. *Vacuum* **2021,** *183,* 109795. doi:10.1016/j.vacuum.2020.109795
5. Sulania, I.; Tripathi, A.; Kabiraj, D.; Varma, S.; Avasthi, D. K. *J. Nanosci. Nanotechnol.* **2008,** *8,* 4163–4167. doi:10.1166/jnn.2008.an13
6. Sulania, I.; Agarwal, D.; Husain, M.; Avasthi, D. K. *Nanoscale Res. Lett.* **2015,** *10,* 88. doi:10.1186/s11671-015-0751-4
7. Ziberi, B.; Cornejo, M.; Frost, F.; Rauschenbach, B. *J. Phys.: Condens. Matter* **2009,** *21,* 224003. doi:10.1088/0953-8984/21/22/224003
8. Ziberi, B.; Frost, F.; Rauschenbach, B. *J. Vac. Sci. Technol., A* **2006,** *24,* 1344–1348. doi:10.1116/1.2188415
9. Sulania, I.; Agarwal, D. C.; Kumar, M.; Kumar, S.; Kumar, P. *Phys. Chem. Chem. Phys.* **2016,** *18,* 20363–20370. doi:10.1039/c6cp03409h
10. Bradley, R. M.; Hofsäss, H. *J. Appl. Phys.* **2016,** *120,* 074302. doi:10.1063/1.4960807
11. Maity, G.; Ojha, S.; Sulania, I.; Devrani, K.; Patel, S. P. *Surf. Interface Anal.* **2019,** *51,* 817–825. doi:10.1002/sia.6655
12. Sulania, I.; Kumar, P.; Priya, P. K.; Bhasker, H. P.; Singh, U. B.; Karn, R. K.; Tyagi, C.; Yadav, R. P. *Radiat. Phys. Chem.* **2022,** *199,* 110353. doi:10.1016/j.radphyschem.2022.110353
13. Facsko, S.; Dekorsy, T.; Koerdt, C.; Trappe, C.; Kurz, H.; Vogt, A.; Hartnagel, H. L. *Science* **1999,** *285,* 1551–1553. doi:10.1126/science.285.5433.1551
14. Stupp, S. I.; Braun, P. V. *Science* **1997,** *277,* 1242–1248. doi:10.1126/science.277.5330.1242
15. Termini, N. C.; Tripathi, J. K.; Hassanein, A. *Thin Solid Films* **2023,** *785,* 140094. doi:10.1016/j.tsf.2023.140094
16. Sulania, I.; Avasthi, D. K.; Tripathi, A.; Hussain, M. *ECS Trans.* **2022,** *107* (1), 3107–3116. doi:10.1149/10701.3107ecst
17. Hofsäss, H. *Appl. Phys. A: Mater. Sci. Process.* **2014,** *114,* 401–422. doi:10.1007/s00339-013-8170-9
18. Hofsäss, H.; Zhang, K.; Gehrke, H. G.; Brüsewitz, C. *Phys. Rev. B* **2013,** *88,* 075426. doi:10.1103/physrevb.88.075426
19. Lopez-Cazalilla, A.; Chowdhury, D.; Ilinov, A.; Mondal, S.; Barman, P.; Bhattacharyya, S. R.; Ghose, D.; Djurabekova, F.; Nordlund, K.; Norris, S. *J. Appl. Phys.* **2018,** *123,* 235108. doi:10.1063/1.5026447
20. Lopez-Cazalilla, A.; Ilinov, A.; Nordlund, K.; Djurabekova, F. *J. Phys.: Condens. Matter* **2019,** *31,* 075302. doi:10.1088/1361-648x/aaf59f
21. Lopez-Cazalilla, A.; Djurabekova, F.; Ilinov, A.; Fridlund, C.; Nordlund, K. *Mater. Res. Lett.* **2020,** *8,* 110–116. doi:10.1080/21663831.2019.1711458
22. Lopez-Cazalilla, A.; Nordlund, K.; Djurabekova, F. *Phys. Rev. Mater.* **2023,** *7,* 036002. doi:10.1103/physrevmaterials.7.036002

23. Norris, S. A.; Samela, J.; Bukonte, L.; Backman, M.; Djurabekova, F.; Nordlund, K.; Madi, C. S.; Brenner, M. P.; Aziz, M. J. *Nat. Commun.* **2011,** *2,* 276. doi:10.1038/ncomms1280
24. Nordlund, K.; Djurabekova, F.; Hobler, G. *Phys. Rev. B* **2016,** *94,* 214109. doi:10.1103/physrevb.94.214109
25. Thompson, M. W.; Nelson, R. S. *Philos. Mag. (1798-1977)* **1962,** *7,* 2015–2026. doi:10.1080/14786436208214470
26. Sigmund, P. *Phys. Rev.* **1969,** *184,* 383–416. doi:10.1103/physrev.184.383
27. Winterbon, K. B.; Sigmund, P.; Sanders, J. *Mat.-Fys. Medd. - K. Dan. Vidensk. Selsk.* **1970,** *37,* 5–73. https://www.researchgate.net/publication/236353890_Spatial_distribution_of_energy_deposited_by_atomic_particles_in_elastic_collisions
28. Carter, G. *J. Phys. D: Appl. Phys.* **2001,** *34,* R1. doi:10.1088/0022-3727/34/3/201
29. Sulania, I.; Tripathi, A.; Kabiraj, D.; Lequeux, M.; Avasthi, D. *Adv. Mater. Lett.* **2010,** *1,* 118–122. doi:10.5185/amlett.2010.5128
30. Keller, A.; Facsko, S.; Cuerno, R. Numerical Integrator for Continuum Equations of Surface Growth and Erosion. In *Computational Nanotechnology Modeling and Applications with MATLAB®;* Musa, S., Ed.; CRC Press: Boca Raton, FL, U.S.A., 2012; pp 189–216. doi:10.1201/9781315217567-5
31. Bradley, R. M.; Harper, J. M. E. *J. Vac. Sci. Technol., A* **1988,** *6,* 2390–2395. doi:10.1116/1.575561
32. Carter, G.; Vishnyakov, V. *Phys. Rev. B* **1996,** *54,* 17647–17653. doi:10.1103/physrevb.54.17647
33. Bøgh, E. *Can. J. Phys.* **1968,** *46,* 653–662. doi:10.1139/p68-081
34. Quéré, Y. *Phys. Status Solidi* **1968,** *30,* 713–722. doi:10.1002/pssb.19680300231
35. Gärtner, K. *Nucl. Instrum. Methods Phys. Res., Sect. B* **2005,** *227,* 522–530. doi:10.1016/j.nimb.2004.10.087
36. Hobler, G.; Nordlund, K. *Nucl. Instrum. Methods Phys. Res., Sect. B* **2019,** *449,* 17–21. doi:10.1016/j.nimb.2019.04.029
37. Chini, T. K.; Okuyama, F.; Tanemura, M.; Nordlund, K. *Phys. Rev. B* **2003,** *67,* 205403. doi:10.1103/physrevb.67.205403
38. Kumar, P. *Semicond. Sci. Technol.* **2016,** *31,* 035014. doi:10.1088/0268-1242/31/3/035014
39. Ziegler, J. F.; Ziegler, M. D.; Biersack, J. P. *Nucl. Instrum. Methods Phys. Res., Sect. B* **2010,** *268,* 1818–1823. doi:10.1016/j.nimb.2010.02.091
40. Kumar, M.; Pandey, R. K.; Pathak, S.; Vandana; Ojha, S.; Kumar, T.; Kumar, R. *Appl. Surf. Sci.* **2021,** *540,* 148338. doi:10.1016/j.apsusc.2020.148338
41. Ruault, M. O.; Chaumont, J.; Bernas, H. *Nucl. Instrum. Methods Phys. Res.* **1983,** *209–210,* 351–356. doi:10.1016/0167-5087(83)90822-0
42. Jones, K. S.; Prussin, S.; Weber, E. R. *Appl. Phys. A: Solids Surf.* **1988,** *45,* 1–34. doi:10.1007/bf00618760
43. Thompson, M. W. *Philos. Trans. R. Soc., A* **2004,** *362,* 5–28. doi:10.1098/rsta.2003.1309

License and Terms

BEILSTEIN JOURNAL OF NANOTECHNOLOGY

Quantum-to-classical modeling of monolayer Ge_2Se_2 and its application in photovoltaic devices

Anup Shrivastava[*1,2], Shivani Saini[1,2], Dolly Kumari[3], Sanjai Singh[2] and Jost Adam[*1,4]

Full Research Paper

Open Access

Address:
[1]Computational Materials and Photonics (CMP), Department of Electrical Engineering and Computer Science, University of Kassel, Kassel, Germany, [2]Computational Nano-Material Research Lab (CNMRL), Indian Institute of Information Technology, Allahabad, Uttar Pradesh, India, [3]Department of Electrical Engineering, Indian Institute of Technology, Patna, India and [4]Center for Interdisciplinary Nanostructure Science and Technology (CINSaT), University of Kassel, Kassel, Germany

Email:
Anup Shrivastava[*] - anup@uni-kassel.de;
Jost Adam[*] - jost.adam@uni-kassel.de

* Corresponding author

Keywords:
2D materials; density functional theory; hole transport layer; optical properties; solar cells

Beilstein J. Nanotechnol. **2024,** *15,* 1153–1169.
https://doi.org/10.3762/bjnano.15.94

Received: 30 April 2024
Accepted: 21 August 2024
Published: 11 September 2024

This article is part of the thematic issue "Smart nanomaterials in electronics and photonics".

Associate Editor: M. H. Kim

Abstract

Since the discovery of graphene in 2004, the unique properties of two-dimensional materials have sparked intense research interest regarding their use as alternative materials in various photonic applications. Transition metal dichalcogenide monolayers have been proposed as transport layers in photovoltaic cells, but the promising characteristics of group IV–VI dichalcogenides are yet to be thoroughly investigated. This manuscript reports on monolayer Ge_2Se_2 (a group IV–VI dichalcogenide), its optoelectronic behavior, and its potential application in photovoltaics. When employed as a hole transport layer, the material fosters an astonishing device performance. We use ab initio modeling for the material prediction, while classical drift–diffusion drives the device simulations. Hybrid functionals calculate electronic and optical properties to maintain high accuracy. The structural stability has been verified using phonon spectra. The *E*–*k* dispersion reveals the investigated material's key electronic properties. The calculations reveal a direct bandgap of 1.12 eV for monolayer Ge_2Se_2. We further extract critical optical parameters using the Kubo–Greenwood formalism and Kramers–Kronig relations. A significantly large absorption coefficient and a high dielectric constant inspired the design of a monolayer Ge_2Se_2-based solar cell, exhibiting a high open circuit voltage of V_{oc} = 1.11 V, a fill factor of 87.66%, and more than 28% power conversion efficiency at room temperature. Our findings advocate monolayer Ge_2Se_2 for various optoelectronic devices, including next-generation solar cells. The hybrid quantum-to-macroscopic methodology presented here applies to broader classes of 2D and 3D materials and structures, showing a path to the computational design of future photovoltaic materials.

Introduction

Reducing fossil fuels and their harmful environmental impact requires improvements in green, sustainable energy sources. Among the various sources of green energy generation, solar energy has been identified as the most promising and expedient because it has the potential to address the current energy demand without making a hazardous impact on the environment [1,2]. Henceforth, researchers have made continuous efforts to design efficient and robust PV devices and solar cells. The systematic study of various solar cells in the last few decades has led to many successful breakthroughs in terms of the stability, efficiency, and cost of PV technology. In the past few decades, perovskite solar cells (PSCs) have emerged as a groundbreaking technology in the field of renewable energy because of their remarkable efficiency and relatively low manufacturing cost [3,4]. These solar cells are based on perovskite-structured compounds, which have demonstrated excellent light absorption, charge-carrier mobilities, and tunable bandgaps [5].

Despite the rapid advancements in PSC technology, some critical issues, such as long-term instability, poor device scalability, and the use of toxic compounds, have yet to be resolved [6]. Recent advancements have seen the integration of two-dimensional (2D) materials with PSCs, opening new avenues for enhancing their performance and addressing current challenges with the PSCs [7,8]. Integrating 2D materials in PSCs can improve their performance. The 2D materials can provide protective layers that work like a shield to the perovskite materials to protect them from environmental degradation caused by moisture and oxygen and provide better device scalability to the PSCs, which makes large-scale production more feasible [9]. Also, the mechanical robustness and flexibility of the 2D materials will give extra room to design the PSCs for a wide range of applications areas [10]. The high carrier mobility and enhanced optoelectronic characteristics can improve the device performance of conventional PSCs [11], and the use of non-toxic 2D materials can improve the performance of PSCs without health risks.

Many researchers recently proposed an ultrathin transport layer-based solar cell as the most expedient photo device for sunlight harvesting. The general scheme of a solar cell comprises various layers including the active/absorber layers, the electron transport layer (ETL) and the hole transport layer (HTL) [12,13]. Both HTL and ETL play a crucial role in achieving a high performance of PV devices. The most common HTL material is spiro-OMeTAD, but it is very expensive [14]. Furthermore, a large number of materials have been reported as ETLs/HTL materials, such as carbon [15], copper iodide [16], $CuSbS_2$, NiO, CuSCN [17], ZnO, and CdS [18]. These materials promote efficient extraction of charge carriers and suppress recombination between the perovskite film and the electrodes. But in all these cases, the transport layer thicknesses are taken as sufficiently high. During the last few decades, researchers claimed that ETLs/HTLs of two-dimensional materials could achieve high power conversion efficiency (PCE) and optimum device performance [18,19]. The key features of the 2D materials, rendering them viable for PV applications were discussed in [20].

Because of the advantages of 2D materials, tremendous efforts have been made to invent highly stable and efficient solar cells based on 2D materials. A number of remarkable works have been recently reported using numerous 2D materials, including MXene's, transition-metal dichalcogenides (TMDCs) and van der Waals structures [21]. Among the various sets of 2D materials, TMDCs (with the general formula of MX_2, where M is a transition metal and X is a chalcogen) attract the broad attention of the research community regarding their extensive applications in photodevices. This is mainly because of the exceptional optoelectronic behavior of the TMDCs, especially the layer-dependent bandgap and the high absorption of incident sunlight [22-25]. Motivated by this, various TMDCs, including MoS_2, WS_2, WSe_2, and TiS_2, have been used in PSCs, either as HTL or as ETL. Yin et al. [26] reported a PCE of approximately 17.3% with TiS_2 nanosheets suspended in isopropanol alcohol in a PSC. 2D sheets of SnS_2 have been proposed by Zhao et al. [27] as a prospective ETL for PSCs. It achieved a maximum PCE of around 20%. Similarly, other PSCs using different 2D layers of TMDCs have been reported (summarized below in Table 3). Despite the pervasive use of TMDC-based 2D materials in solar cells, their device performance still leaves room for improvement.

Recently, a new class of dichalcogenides (group IV–VI metal chalcogenides) has been successfully synthesized [28-31]. Its remarkable features, such as low cost, abundance, environmental friendliness, and many interesting physical properties, indicate a broad range of possible applications in sustainable electronics and photonics [32]. Notably, a high absorption coefficient has been reported in [33] for an SnS monolayer across the direct absorption edge at 1.3–1.5 eV, rendering it potentially applicable in solar cells and photodetectors. Similarly, Huang et al. [34] showed that a band transition (from indirect to direct) occurs in $SnSe_2$ when moving from bulk to monolayers, elucidating its application potential in optoelectronic devices. More group IV–VI dichalcogenides have been discussed in [35-40] for different applications. Although some inceptive work has been done using monolayers of metal dichalcogenides, there are still plenty of opportunities to explore. In line with the same,

we have studied the thermoelectric behavior of monolayer Ge_2Se_2 in our previous work [41].

This article aims to investigate the optoelectronic properties of the group IV–VI dichalcogenide monolayer Ge_2Se_2 using density functional theory (DFT) and to demonstrate its potential application in photovoltaic solar cells. The proposed Ge_2Se_2 monolayer exhibited excellent thermodynamic stability, higher carrier mobilities (due to the presence of valleys in the CB/VB), and good optical response (an interband transition in the visible region). Considering the proper design criteria and selecting an appropriate material for absorbers/ETL, we have designed and modeled the solar cell in a FTO–TiO_2–$CsSn_{0.5}Ge_{0.5}I_3$–Ge_2Se_2–Ag configuration, which outperforms, in terms of their key parameters, other reported works in the literature. The proposed solar cell configuration is environmentally friendly (absence of toxic materials), of low cost, and highly efficient. The computational methodology followed here is depicted in Figure 1, and we provide detailed corresponding instructions and references in the Methods section.

Results and Discussion

The computational approach can be better explained by separating it into two subsections, namely (a) material simulation using DFT and (b) device simulation using a macroscopic approach, which will be discussed in section Computational Methods.

Structural and stability analysis

The schematic atomistic model for monolayer Ge_2Se_2 is shown in Figure 2. For better understanding, a side view of monolayer Ge_2Se_2 with the corresponding lattice parameters is given in Figure 2a, and the top view of the supercell of the order 4×4 is shown in Figure 2b. From Figure 2a, we can observe that the unit cell of monolayer Ge_2Se_2 consists of four atoms (two for each Ge and Se). More precisely, we can observe two sublayers corresponding to a crystallogen (Ge) and a chalcogen (Se), which are designate as top and bottom moieties. From Figure 2, we can also notice that the structure of monolayer Ge_2Se_2 is identical to the puckered phosphorene (simple orthorhombic structure) with space group symmetry of $Pmn2_1$ (C_{2v}^7) in 2D space.

The geometry-optimized lattice parameters a and b are found to be 4.13 and 3.99 Å, respectively. The bond lengths between consecutive crystallogen and chalcogen (Ge–Se) are 2.59 and 2.67 Å in the horizontal and vertical directions, respectively. All optimized structural parameters excellently match with previously reported values [41,42]. In addition to the lattice parameters for the monolayer Ge_2Se_2, we have optimized the vacuum slab in a normal direction to avoid interlayer interactions. The

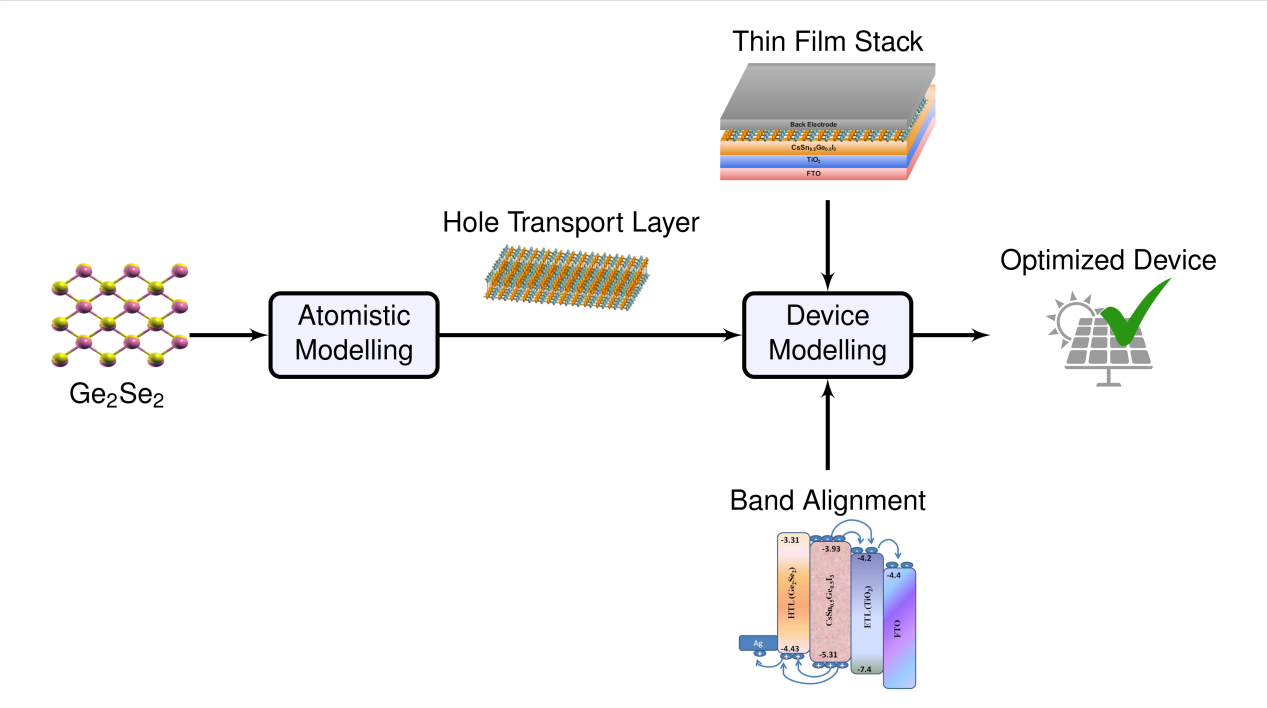

Figure 1: Optoelectronic property investigation of a group IV–VI dichalcogenide monolayer (Ge_2Se_2), and its application potential for hole transport layers in Ge_2Se_2/$CsSnGeI_3$/TiO_2-based solar cells. Our computational approach combines density functional theory and atomistic modeling with (macroscopic) device modeling to obtain an otimized device performance.

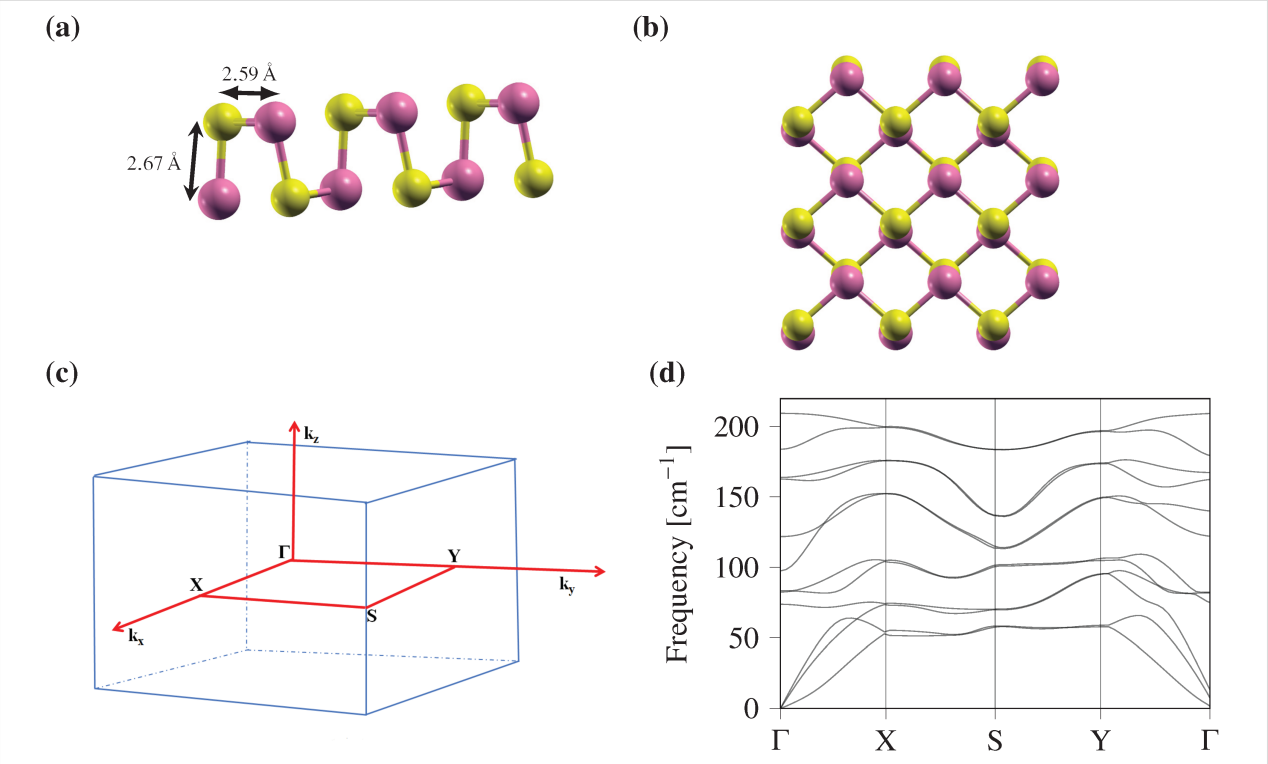

Figure 2: Geometry and stability of Ge_2Se_2 monolayers. (a) Side view with the corresponding structural parameters and (b) top view. The exhibited structure is a simple orthorhombic structure with space group symmetry of *Pmn*2$_1$ (C_{2v}^7) in 2D space. (c) Brillouin zone, where the Γ-X-S-Y-Γ path is used to plot the phonon spectra, and (d) phonon dispersion, confirming the structure's dynamical stability (Figure 2a,b were redrawn from [41], Figure 2d was re-plotted from [41]).

optimized vacuum level was found to be 23 Å. Furthermore, to test the stability of the crystal structure, we have computed the phonon band dispersion for monolayer Ge_2Se_2 within the first Brillouin zone (Figure 2c). The calculated phonon spectra along the high symmetry path Γ-X-S-Y-Γ in the first Brillouin zone are shown in Figure 2d.

The phonon spectrum for monolayer Ge_2Se_2 has twelve vibrational modes, of which three are acoustical (low-frequency) modes (transverse acoustic, longitudinal acoustic, and flexural acoustic). The remaining nine (high-frequency) modes correspond to optical modes. The flexural acoustic mode is an out-of-plane transverse acoustic mode, similar to those in other two-dimensional materials such as graphene, phosphorene, and stanene, demonstrating a quadratic nature near the Γ point [43-45]. Figure 2d clearly depicts that all phonon bands throughout the spectrum have non-imaginary frequency, further confirming the investigated structure's dynamic stability.

Electronic and transport properties

The electronic properties of materials play a crucial role in predicting the material behavior and transport parameters and, hence, its prospective applications. We investigated the electronic properties of monolayer Ge_2Se_2 using its electronic band structure and density of states, as shown in Figure 3. To maintain a high degree of accuracy, we calculated the band structure using the HSE06 functional, and the band dispersion along the high symmetry paths Γ-X-S-Y-Γ in the first Brillouin zone, as shown in Figure 3.

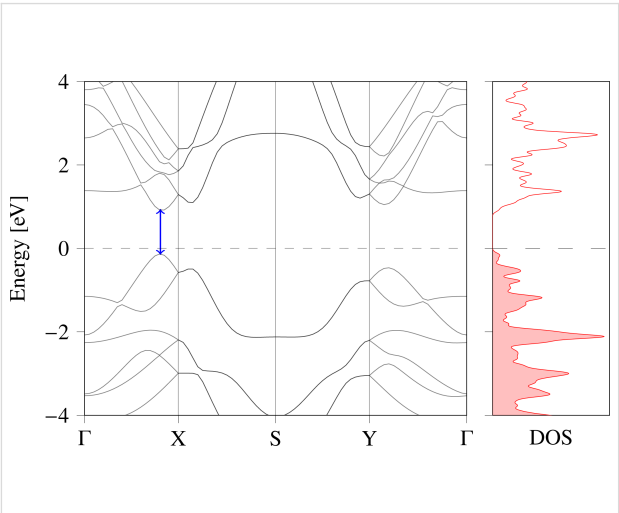

Figure 3: The electronic band structure of monolayer Ge_2Se_2, revealing a direct bandgap of 1.12 eV, and the corresponding density of states (The electronic band structure was re-plotted from [41]).

Figure 3 depicts that the monolayer Ge_2Se_2 is a direct-bandgap semiconductor with a bandgap of the order of 1.12 eV. Valence band maximum (VBM) and conduction band minimum (CBM) are located along the Γ-X path. The computed bandgap value and its dispersion nature are consistent with earlier reported works [41,42,46,47]. The optimum bandgap value and its CBM/VBM positions make it suitable for photovoltaic applications and provide a guideline for selecting the absorber layers in the solar cells. Notably, multivalley and flat bands are present in the energy band structure. The formation of multiple valleys provides extra carrier pockets for transportation, further increasing carrier mobility. Also, the larger valley degeneracy will increase the density of states (DOS) effective mass without influencing the carrier mobility. We have also calculated the total DOS to understand and justify the band structure calculation. Figure 3 shows that the calculated DOS is consistent with the electronic band structure and the bandgap values, further validating the results.

Other properties that will be useful in the simulation of solar cells, such as the effective mass of charge carriers (electrons/holes), conduction/valence band density of states, electron/hole mobility, electron affinity, and work function can be derived from the initial band energy calculation.

We calculated the effective masses of electrons and holes as $m_e^* = 0.167m_e$ and $m_h^* = 0.1768m_e$, respectively, which are very close to the values ($m_e^* = 0.17m_e$, and $m_h^* = 0.17328m_e$) reported in the literature [46,47]. With that, we estimated the effective DOS values in the CB and the VB to be 0.1732×10^{19} /cm^3 and 0.1887×10^{19} /cm^3, respectively. The electron and hole thermal velocities for monolayer Ge_2Se_2 were estimated as 9.43×10^5 m/s and 2.668×10^5 m/s, respectively. The predicted charge carrier mobilities were found to be 187.003 cm^2/(V·s) and 300.451 cm^2/(V·s) for holes and electrons, respectively. The high carrier mobility further suggests a potential application as a transport layer in solar cells as well as in the channel materials of FETs. It is important to note that although in the case of solar cells, the transmission of charge carriers takes place in the out-of-plane direction, which is usually considered to be low compared to the in-plane mobility (especially in the bulk materials), the charge carriers still move quickly across the thin HTL because of the ultrathin layer and the strong electric field gradient from the active layer to the electrode. Finally, higher in-plane mobility of the monolayers can compensate the potential limitations of out-of-pane mobility for its prospective uses in solar cells, V-FETs, TFETs, and memristors [48].

In the present calculation, we have calculated the average planar electrostatic potential along the plane as demonstrated in Figure 4. The figure depicts the vacuum energy level and the positions of HOMO and LUMO. The calculated work function and electron affinity for monolayer Ge_2Se_2 are about 3.313 and 3.873 eV, respectively, which are comparable with previously reported values of 3.39 eV and 3.9 eV [46,47].

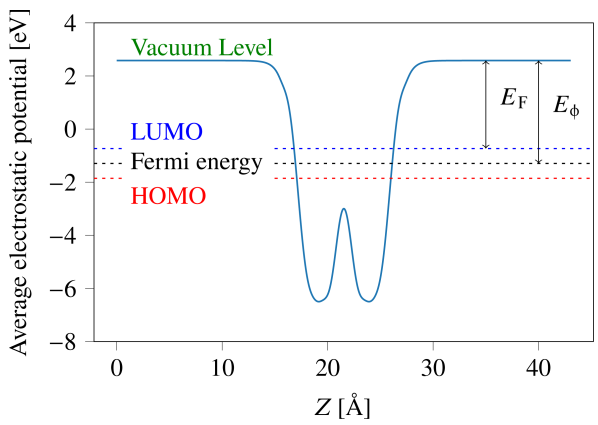

Figure 4: Macroscopic potential distribution vs lattice vector in the normal direction for monolayer Ge_2Se_2. In a periodic system, the electron affinity and work function is defined as EA = $E_{Vac} - E_{LUMO}$, and $E_\phi = E_{Vac} - E_F$, where E_F is the Fermi energy level, E_ϕ is the work function, EA is the electron affinity, E_{Vac} is the vacuum energy level, and E_{LUMO} is the LUMO energy level, respectively. The calculated work function and electron affinity are about 3.313 and 3.873 eV, respectively.

A high degree of agreement for all estimated electronic parameters with earlier reported values validates the accuracy of our computation.

Optical properties

As discussed in the previous section, monolayer Ge_2Se_2 has structural stability and exhibits an optimal electronic behavior with a direct bandgap of 1.12 eV. The DFT results indicate potential applications of the investigated structure in optoelectronic devices. The optical responses at varying photonic energies and the corresponding optical wavelength are summarized in Figure 5, depicting the dielectric function ε_r (real and imaginary parts) and the refractive index n for monolayer Ge_2Se_2. The real and imaginary components of the dielectric function correspond to dispersive and absorption effects of the material. We observe that the investigated structure exhibits strongly anisotropic optical properties for which the parametric values depend on the direction of the chosen plane.

Dielectric function and absorption coefficient

The static dielectric constants (real part of ε_r at $\omega = 0$), along the in-plane (XX) and out-of-plane (ZZ) direction were calculated as 6.37 and 2.4, respectively, suggesting that monolayer Ge_2Se_2 is highly polarized along the in-plane direction.

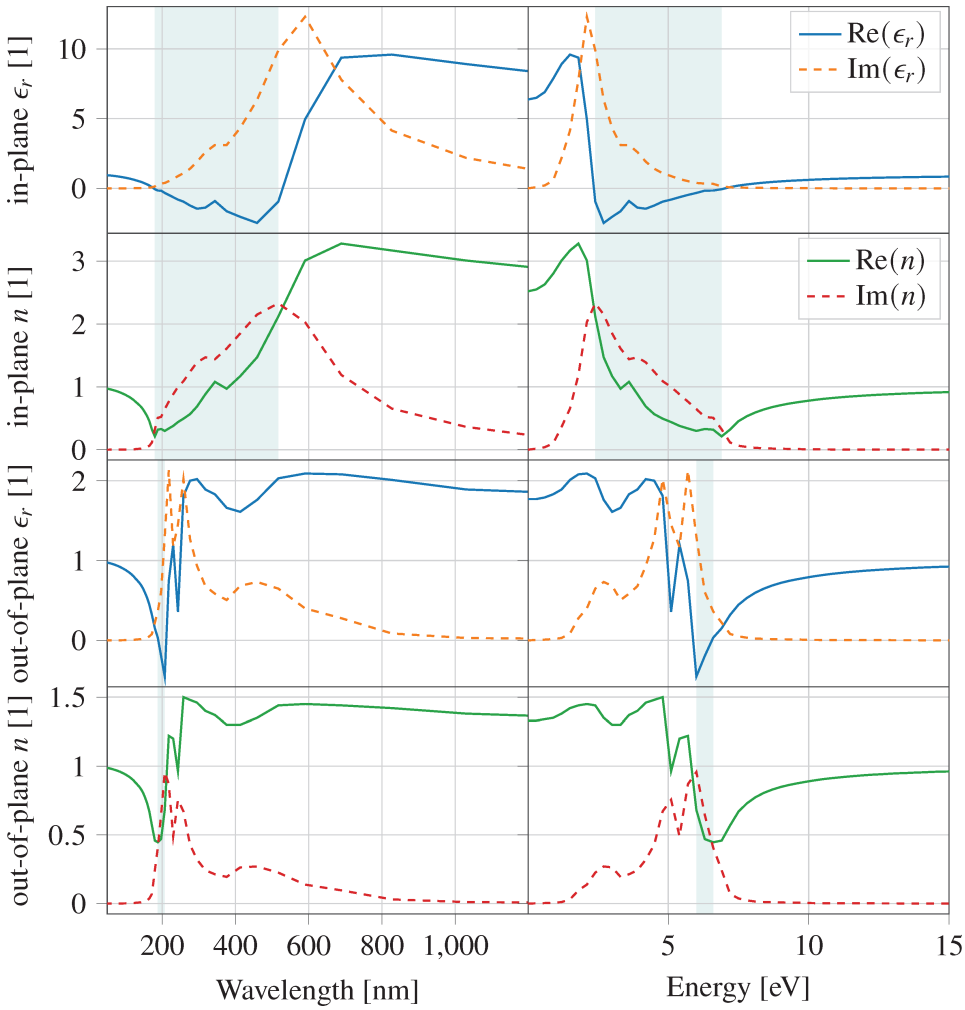

Figure 5: Optical responses of monolayer Ge_2Se_2; real (solid) and imaginary (dashed) part of the dielectric constant and refractive index vs wavelength (left) and photon energy (right), for in-plane and out-of-plane excitation relative to the sheet. The teal-colored areas mark the regions of potential metallic behavior (Re(ε_r) < 0 or, equivalently, Re(n) < Im(n)), occurring between 180 and 517 nm (2.4 and 6.9 eV) for in-plane, and between 188 and 207 nm (6.0 and 6.6 eV) for out-of-plane excitation.

The imaginary part of the dielectric function shows peaks between 2 and 3 eV, along the XX direction, which indicate an interband transition in the visible region (Figure 5). Interestingly, we can observe tracking bands (the region where the energy difference between the conduction and valence bands is approximately constant [49]) around the high-symmetry point S and between X and Y in the first Brillouin zone. Around these points, we notice a small gradient and, thus, large DOS, which further leads to higher transition possibilities.

The absorption coefficient elucidates the rate at which light intensity diminishes while entering the material. It primarily depends upon the imaginary part of the refractive index $k(\lambda) = \mathrm{Im}\{n(\lambda)\}$ and the wavelength of the incident light λ, as per $\alpha_{abs} = 4\pi k(\lambda)/\lambda$. The highest peak of the absorption coefficient lies in the visible region, which we attribute to the direct transition from VBM to CBM. The other peaks correspond to the transition from the top valence band to the conduction band in a band region of the Brillouin zone around the S point. The maximum absorption coefficient is 5×10^5 cm^{-1} along the XX direction. The highest peak for the ZZ direction is calculated as 5.8×10^5 cm^{-1}, corresponding to the UV region. We attribute this maximum to the transition from VBM to CBM, while the other peaks designate a transition from VBM to CBM around a wide range of spectra at the S point.

Refractive index and extinction coefficient

The real part of the material's refractive index defines the angle of refraction that the light undergoes while entering a medium. Higher refractive indices refer to lower refraction angles measured from the interface normal. The static refractive indices for monolayer Ge_2Se_2 in the direction parallel to the

plane (XX) and normal to the plane (ZZ) are approximately 2.5 and 1.4, respectively, as shown in Figure 5. These refractive indices could enable the use of the investigated material as an inner layer coating between the absorber and substrate/electrodes in the design of solar cells.

Device Modeling

The high carrier mobility, optimum bandgap, and suitable optical characteristics of monolayer Ge_2Se_2 as discussed in the previous section, further motivated us to design a photovoltaic solar cell using monolayered Ge_2Se_2. The easy fabrication, structural stability, and proper band alignment with the absorber material make it a promising hole transport layer (HTL) in the proposed solar cell. The proposed solar cell is a low-cost, environmentally friendly, scalable Perovskite solar cell (PSC), with Ge_2Se_2 as a HTL. The schematic of the proposed solar cell is shown in Figure 6a.

The proposed structure consists of a lead-free Perovskite layer as an absorber, titanium dioxide (TiO_2) as ETL, and Ge_2Se_2 as HTL. A 100 nm thick layer of FTO is used to encapsulate the transport and absorber layers and treated as a conductor in this simulation. Regarding an absorber material corresponding to the proposed HTL, a minimum valence band offset between these two layers has been considered as a necessary condition for achieving optimum performance. In addition to this, environmental friendliness, stability, and cost-effectiveness were also considerations to choose $CsSn_{0.5}Ge_{0.5}I_3$ as an absorber layer. After selecting the absorber layer, the ETL has been chosen based on a matching conduction band offset with the absorber layer and the high electron mobility. Among the various options, TiO_2 offers minimum band offset and ease of synthesis. The front and back contacts are supposed to be ohmic and are made of silver (Ag) to maintain proper band alignment and reduce the band offset. It has been reported that tuning the CBM and VBM positions to keep a low band offset leads to superior device performance. Figure 6b exhibits the position of CBM/VBM in consecutive layers of the proposed structure. This further demonstrates the ease of charge transfers from the absorber to the respective transport layers.

The thickness and other simulation parameters for the active layer and the ETL were taken from the literature [17,50,51], while all the simulation parameters for Ge_2Se_2 have been derived from the DFT calculations as discussed in the previous section. All simulation parameters are summarized in Table 1

Performance estimation

Using the proposed model, we have estimated the performance of the solar cell in terms of open-circuit voltage (V_{oc}), short-circuit current density (J_{sc}), fill factor (FF), and power conversion efficiency (η). The performance of solar cells largely depends on various parameters, including the thickness of transport layers, absorber layers, and absolute temperature. Therefore, to get the optimum performance of the proposed device, we have optimized the performance of the cell module by varying the layer thicknesses of HTL, ETL, and absorber. Also, we have tested the performance of the device under the influence of varying defects densities in the active layer and the interfaces. The optimization corresponding to different parameters is summarized in the following sections.

Effect of HTL thickness variation

While the absorber layer is the crucial component of a solar cell, the role of the HTL cannot be overlooked because the choice of HTL plays a significant role in ensuring efficient charge transport, reducing recombination losses, and overall device stability. Therefore, numerous efforts have been made in

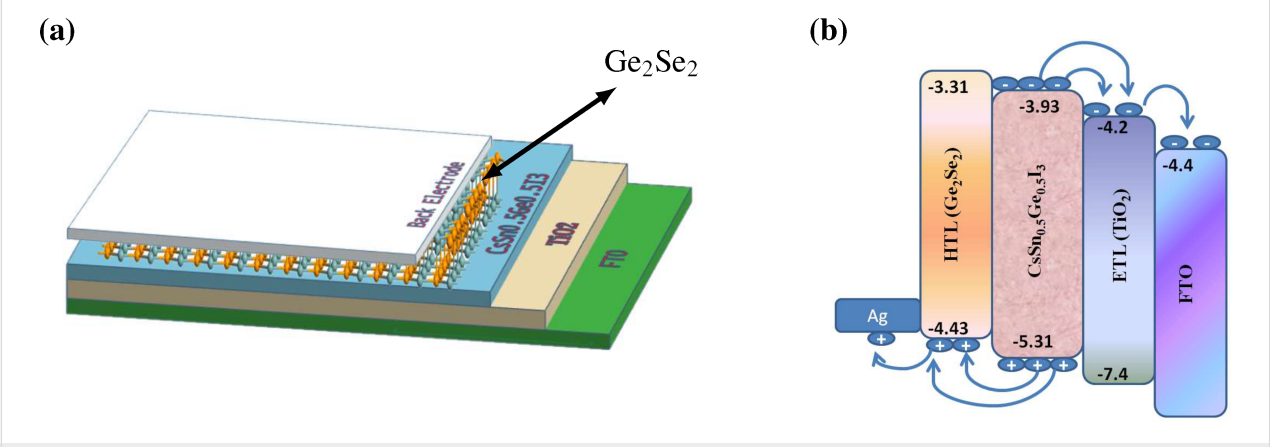

Figure 6: Schematic of the proposed PSC using Ge_2Se_2 as HTL; (a) device setup consisting of stacked layers of FTO–TiO_2–$CsSn_{0.5}Ge_{0.5}I_3$–Ge_2Se_2–Ag; (b) band offset among different PSC layers, demonstrating the ease of charge-transfer from the active layers to the respective transport layers.

Table 1: Simulation parameters for the proposed PSC.

Device parameter	FTO [50]	Ge_2Se_2 [our calculations]	$CsSn_{0.5}Ge_{0.5}I_3$ [51]	TiO_2 [17]
Bandgap (E_g) (eV)	3.4	1.12	1.5	3.26
Electron affinity (eV)	4.5	3.31	3.9	4.2
Dielectric constant (ε_r)	9.1	6.37	28	10
Conduction band effective DOS (cm^{-3})	1.1×10^{19}	0.1732×10^{19}	1.0×10^{19}	2.0×10^{17}
Valence band effective DOS (cm^{-3})	1.1×10^{19}	0.1887×10^{19}	1.0×10^{19}	6.0×10^{17}
Electron thermal velocity ($m \cdot s^{-1}$)	1×10^7	9.47×10^5	1×10^7	1×10^7
Hole thermal velocity ($m \cdot s^{-1}$)	1×10^7	2.66×10^5	1×10^7	1×10^7
Electron mobility ($cm^2 \cdot V^{-1} \cdot s^{-1}$)	20	300.451	974	100
Hole mobility ($cm^2 \cdot V^{-1} \cdot s^{-1}$)	10	187.003	213	25

the past to investigate suitable HTL materials for efficient solar cells [52-54]. The main function of the HTL is to capture the holes generated from the absorber layer and transfer them to the respective electrode. The thickness of the HTL also influences the device performance significantly. To optimize the HTL thickness for optimal device performance, we assumed a layer thickness of monolayer Ge_2Se_2, ranging from 1 to 10 nm. Figure 7a depicts the change of the performance parameters upon varying the HTL thickness.

It can be observed from Figure 7a that the device parameters decrease with higher HTL thickness. This behavior is mainly due to the appearance of a higher series resistance at larger HTL thicknesses. Also, a thick HTL may increase the chances of charge carrier recombination. Nevertheless, the performance degradation is very slight because of the ultrathin HTL layer proposed here. It is worth mentioning that there is an incremental rise in the short-circuit current density with thicker HTL. This is due to less carrier losses owing to reduced recombination at the interface of HTL and absorber layer and better surface cleavage because of the thick HTL [55,56]. Figure 7a indicates that 1 nm of HTL yields superior performance in terms of PCE, V_{oc}, J_{sc}, and FF with values of 28.148%, ≈1.11 V, 28.70 $mA \cdot cm^{-2}$, and ≈87.77% FF, respectively.

Effect of ETL thickness variation

In conjunction with the HTL, the ETL is responsible for collecting electrons generated in the active absorber layer. It is also necessary to optimize the ETL thickness to get an optimal device behavior. The change of the device parameters with varying ETL thickness is shown in Figure 7b. A higher thickness of the ETL leads to a worse device performance. When the layer thickness increases, the series resistance in the cell will also increase, and the light transmittance through the ETL decreases. The latter affects photogeneration in the perovskite layer, reducing J_{sc} and, consequently, the cell efficiency. Also, one can notice that the fill factor initially increases and then decreases mainly due to the small reverse saturation current for lower values of the ETL thickness. Later on, at higher ETL thicknesses, the fill factor decreases with increase in series resistance, and the cell efficiency decreases [57]. Since the ETL thickness is low, the impact on the performance degradation is insignificant. After examining all parameters, we found an optimized ETL thickness of 20 nm in our proposed device. The optimized values of the solar cell parameters at the optimal ETL thickness are 28.11%, ≈1.11 V, 28.68 $mA \cdot cm^{-2}$, and ≈87.81% for PCE, V_{oc}, J_{sc}, and FF, respectively.

Effect of absorber thickness variation

The absorber layer thickness is the most important and critical device parameter. The role of the absorber layer is to absorb the photons and generate charge carriers required for the current flow. It is intuitive to have a thick absorber layer for a higher current density. However, because the absorber thickness further affects the recombination rate, optimizing it for optimal device performance is necessary. The impact of varying absorber thickness on the different device parameters is summarized in Figure 7c. The absorber layer thickness was varied from 1 to 10 μm to obtain the optimal performance of the proposed device. Figure 7c shows that the short-circuit current density (J_{sc}) increases with higher absorber thickness up to a thickness of 4 μm, before reaching a constant value. The maximum short-circuit current density (J_{sc}) was calculated as 28.86 $mA \cdot cm^{-2}$ corresponding to an absorber thickness of 4 μm. The current variation followed the Beer–Lambert law, which justifies that more absorption will occur when the thickness of the absorber layer increases. A thicker absorber layer allows more photons to get absorbed, which leads to the generation of more electron–hole pairs. These generated electron–hole pairs, collected by the respective transport layers, contribute to the higher current density [58].

It is worth noticing that there is a significant impact of the absorber thickness on almost all parameters. The PCE increases

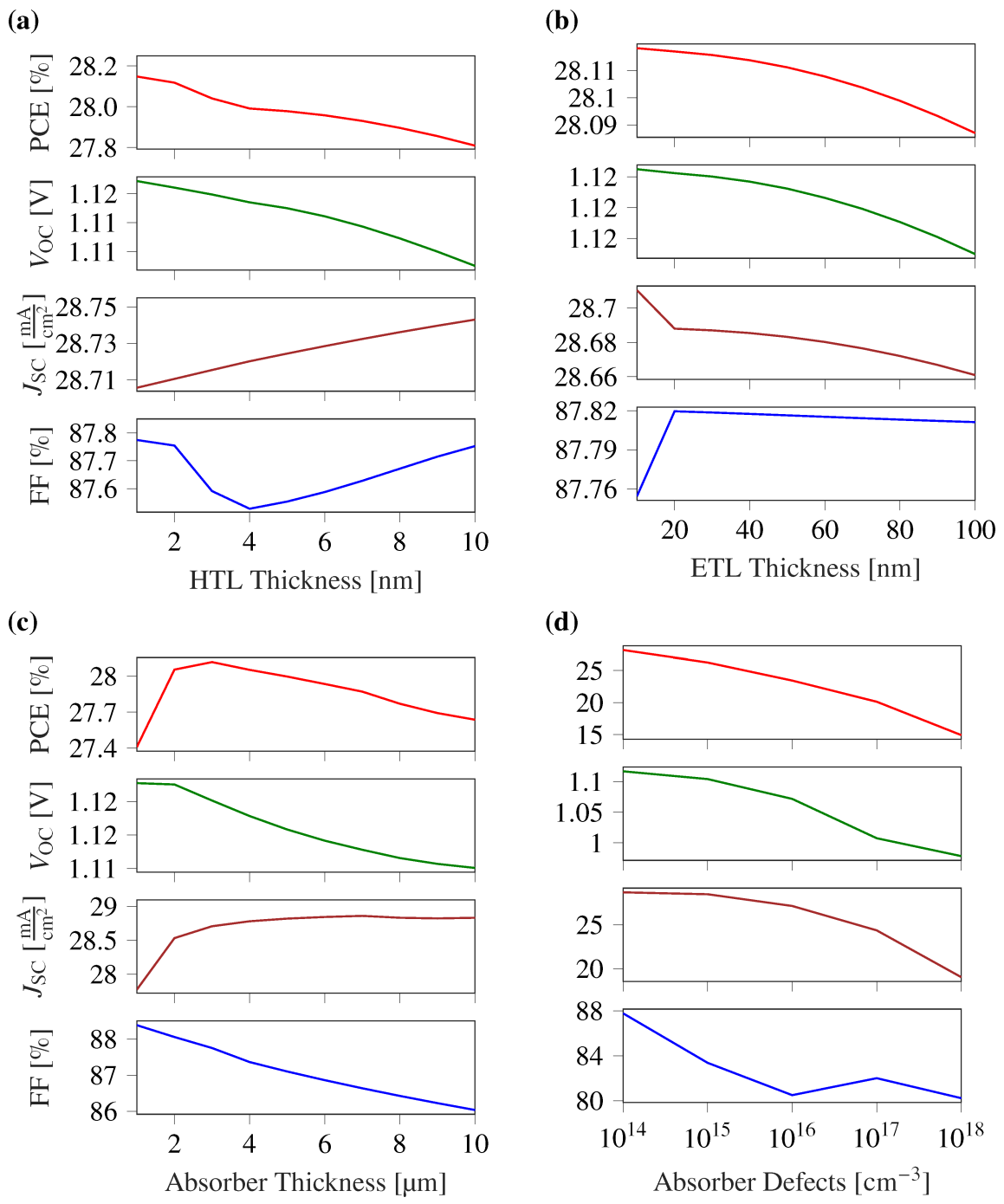

Figure 7: PSC performance parameters as functions of (a) HTL thickness, (b) ETL thickness, (c) absorber thickness, and (d) absorber defects. The device exhibits optimal performance at layer thicknesses of ETL, absorber, and HTL of 20 nm, 2 µm, and 1 nm, respectively.

from 27.4% to 28.11%, and the short-circuit current J_{sc} value reaches up to 28.86 mA·cm^{-2}. We observed that there is a significant reduction in FF and V_{oc} at higher absorber thicknesses, primarily because of the increasing series resistance and higher losses [59]. We set the optimal absorber thickness at 2 µm, above which the parameter variation was only very little.

Effect of defects in the absorber layer

Halide pervoskites are generally considered as defect-resilient; yet, deep level defects shows significant impact on the device performance [60,61]. Therefore, it is important to analyze their impact on the cell performance for better device design. Figure 7d shows the variation of the cell parameters at varying

absorber defect densities from 10^{14} cm^{-3} to 10^{18} cm^{-3}. Figure 7d shows that higher defect densities lead to worse device performance. This is due to the decrement in the lifetime of the charge carriers because of the shorter diffusion length, which results from the higher defect densities [62]. We can observed that the performance parameters decrease significantly above defect densities of 10^{15} cm^{-3}.

Effect of interface defects between active and transport layers

The photovoltaic behavior of halide perovskites is significantly affected by the properties of the interfaces. This is because a majority of defects arises at the junction between two layers during the fabrication of the device, caused by mismatches in the lattice structures, which lead to dangling bonds. These defects at the junctions play a critical role in the performance of the device as they contribute to increased local recombination at the interface. Within this particular PSC, two critical interface layers exist, namely, the interface between the absorber and the ETL and the interface between the absorber and the HTL. We analyzed the device performance by varying the defect densities at both interfaces within the range of 10^{6} cm^{-3} to 10^{15} cm^{-3}. Because of the ultrathin HTL layer, the absorber/HTL interface is more sensitive, and the device performance is anticipated to degrade above interface defect densities of 10^{7} cm^{-3}. However, the ETL/absorber interface exhibits excellent performance up to interface defects of 10^{12} cm^{-3} (Table 2), after which the device performance starts to deteriorate (Figure 8).

Table 2: Performance of the proposed PSC under 1.5G solar illumination.

Device parameter	Value
Open circuit voltage (V_{oc})	1.11 V
Short circuit current density (J_{sc})	28.70 mA·cm^{-2}
Fill factor (FF)	87.66%
Power conversion efficiency (PCE)	28.10%

The computed current density vs voltage curve is shown in Figure 9a, and the energy band diagram corresponding to the different layers is demonstrated in Figure 9b. We have also compared the proposed device with the combination of different transport layers in Table 3. It demonstrates that the proposed PSC structure excels in terms of performance parameters compared to other reported structures.

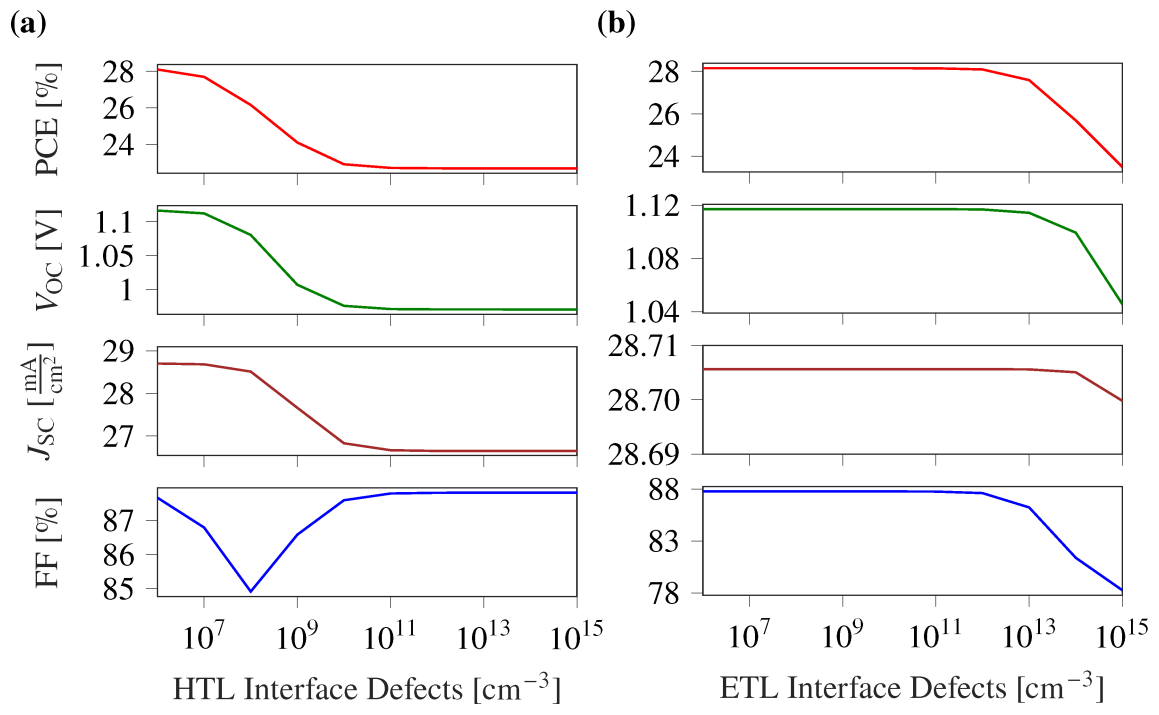

Figure 8: Variation of PSC performance parameters with interface defects between (a) ETL and active layer, and (b) active layer and HTL. Because of the ultrathin HTL layer, the interface at the absorber/HTL is more sensitive, and the device performance degrades for interface defect densities above 10^{7} cm^{-3}. However, the ETL/absorber interface exhibits an excellent performance up to the interface defects of 10^{12} cm^{-3}, after which the device performance starts to deteriorate.

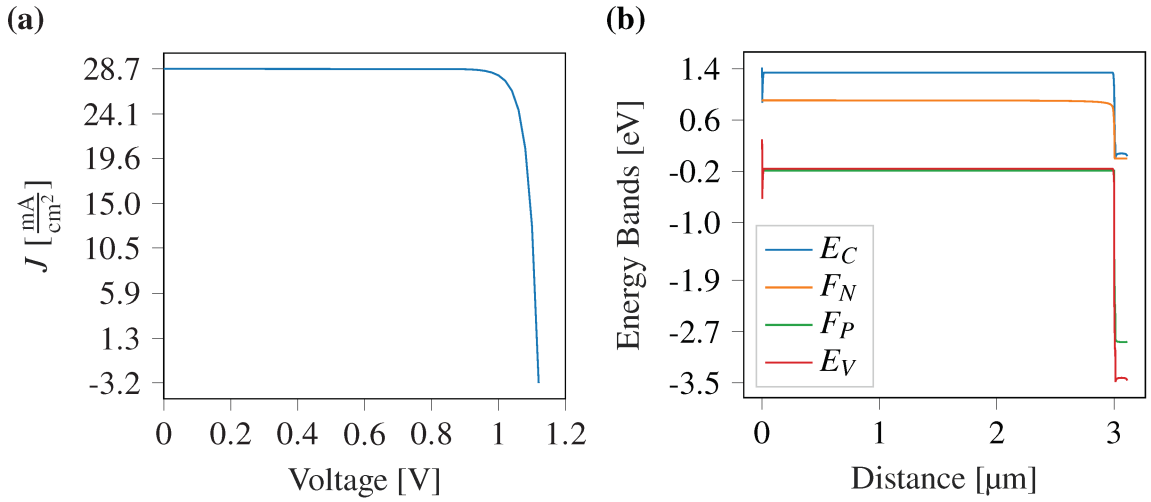

Figure 9: (a) Current density vs voltage curve for the proposed PSC, demonstrating a short-circuit current density and an open-circuit voltage of 28.7 mA·cm^{-2} and 1.11 V, respectively. (b) Energy band diagram for the proposed solar cell, where E_C stands for conduction band and E_V stands for valence band. F_N and F_P stand for quasi-Fermi levels of electrons and holes, respectively, at T = 300 K.

Table 3: Comparison of the PSC performance with earlier reported works.

Device configuration	V_{oc} (V)	J_{sc} (mA·cm^{-2})	FF (%)	PCE (%)
Ag/TiO_2/PSK/MoS_2/ITO [19]	0.93	26.24	83.0	29.43
Au/Cu_2O/PSK/TiO_2/FTO [63]	0.96	15.8	59.0	8.93
Au/MoS_2/PSK/WS_2/FTO [64]	0.96	27.3	87.62	22.17
Au/Spiro–OMeTAD/PSK/TiS_2/FTO [26]	0.95	20.05	66.90	12.75
Ag/Ge_2Se_2/PSK/TiO_2/FTO [This work]	1.11	28.70	87.66	28.10

Computational Methods

The methodology presented here (illustrated in Figure 10) is more generally valid and will apply to broader classes of 2D and 3D materials and structures. Therefore, we believe this section might serve as a mini tutorial for the computational design of future photovoltaic materials.

Material simulation using DFT

The structural and electronic properties have been investigated using an ab initio computational approach within the density functional theory (DFT) framework as implemented in the Quantum Espresso (QE) code [65,66].

We started our calculation to relax the structure at its most stable state (minimum energy) using the Broyden–Fletcher–Goldfarb–Shanno (BFGS) algorithm for a systematic computational study. It has been reported that the hybrid functional is more accurate in predicting the material behavior than local density approximation (LDA) [67] or generalized gradient approximation (GGA) [68] for modeling the exchange–correlation. Hence, for greater accuracy, we have used the Perdew–Burke–Ernzerhof (PBE) [69] and Heyd–Scuseria–Ernzerhof (HSE06) [70] functionals to model the exchange–correlation interactions with a screening parameter of 0.1 and mixing parameters of 25%. An ultrasoft, scalar relativistic pseudopotential of Troullier–Martins type [71] has been used to model the core corrections in the calculations. The valence electronic configuration for Ge and Se is taken as $4s^24p^23d^{10}$ and $4s^24p^43d^{10}$, respectively, and all electron-like wave functions have been generated using the projected augmented wave (PAW) method. A plane-wave basis set has been used to consolidate the interaction between core and valence electrons with an optimized threshold energy of 60 Ry. For efficient and precise calculations, the Brillouin zone has been sampled into 13 × 13 × 1 K-mesh points (using the Monkhorst–Pack scheme [72]) and high-energy/force convergence criteria of 10^{-10} eV/10^{-10} eV/Å^3, respectively, have been set for two consecutive self-consistent cycles. A sufficiently high vacuum of 23 Å is applied perpendicularly to avoid interlayer interactions.

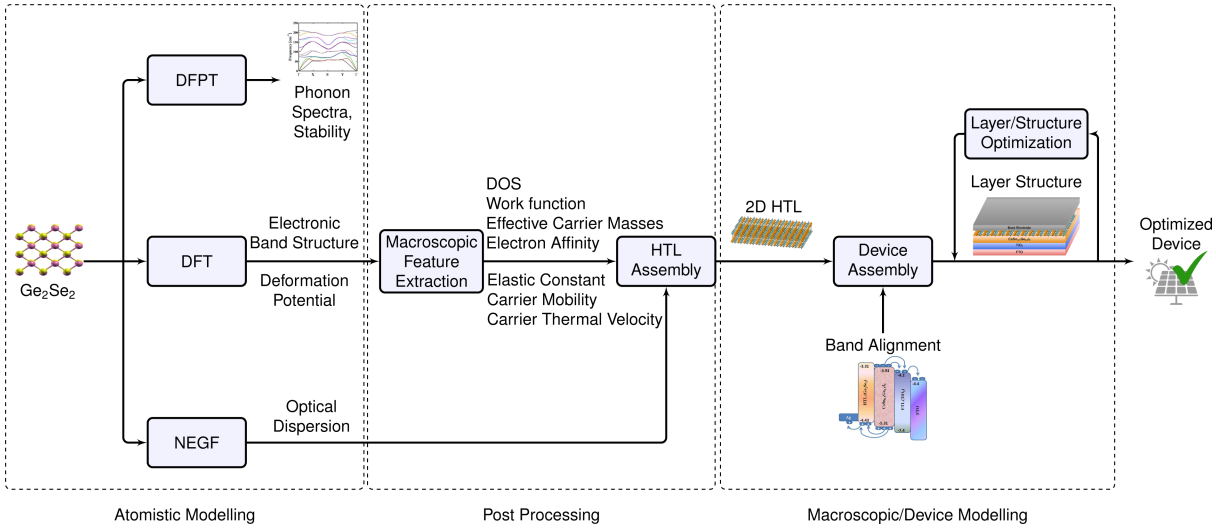

Figure 10: Computational pathway to estimate the materials' behavior and application in a PSC. First step – DFT geometry optimization, optimization of computational parameters, and electronic band structure and deformation potential extraction. Second step – test of the structural stability via density functional perturbation theory (DFPT): We compute the phonon spectra to verify the structure's dynamical stability. Third step – DFT-based electronic property estimation: We utilize the HSE functional to predict the band structure. Fourth step – DFT post-processing: (a) Extraction of the device-related parameters such as DOS, charge mobility, effective masses, thermal velocities, electron affinity, and work functions from fundamental physics equations together with DFT-post processing; (b) calculation of the optical behavior based on the non-equilibrium Green's function (NEGF) and the Kubo–Greenwood approaches. Fifth step – device design, simulation, and optimization: After proper band alignment and suitable material choices for the transport and active layers, we design a stacked solar cell, simulate it (in the SCAPS simulator), and optimize the individual layers for the best device performance.

The stability of the Ge_2Se_2 monolayer was estimated by phonon dispersion. The phonon dispersion has been calculated using density functional perturbation theory (DFPT), as implemented in the QE package. To compute the phonon spectra, we have estimated the second-order interatomic force constant using the relation [73]:

$$\Phi_{\alpha\beta} = \frac{\partial^2 \phi}{\partial r_\alpha \partial r_\beta}. \quad (1)$$

To maintain high accuracy, a large plane-wave mesh cutoff of 120 Ry is considered throughout the calculations.

Extraction of device-relevant parameters

To design a solar cell, we can derive some parameters from the DOS and *E*–*k* dispersion curves, such as the effective masses of electrons (m_e^*) and holes (m_h^*), the effective DOS in the conduction and valence bands (N_c and N_v), electron and hole thermal velocities (V_{th_e} and V_{th_h}), electron and hole mobilities, electron affinity, and work function. We outline an efficient approach to calculating these device parameters briefly below.

According to the *K*–*P* model, the charge carrier effective masses are given as $m^* = \frac{1}{\hbar^2}[\frac{\partial^2 E}{\partial k^2}]^{-1}$, where $\hbar$ is the reduced Plank constant, E is the charge carrier's energy, and k is a wave vector. To estimate the effective masses of electrons and holes, we used a curve-fitting algorithm (weighted least squares method) within a small parabolic section of the conduction band minima (CBM) and valence band maxima (VBM).

Using the charge carriers' effective masses, the effective DOS in the conduction and valence bands can be estimated as [74,75]:

$$N_c = 2\left[\frac{2\pi m_e^* k_B T}{\hbar^2}\right]^{3/2} \text{ and } N_v = 2\left[\frac{2\pi m_h^* k_B T}{\hbar^2}\right]^{3/2}, \quad (2)$$

where N_c and N_v are the effective DOS in the CB and VB, respectively, and the charge carriers' effective masses are m_e^* and m_h^* for electrons and holes, respectively. k_B, and T denote the Boltzmann constant and the absolute temperature, respectively.

We also calculated the electron and hole thermal velocities using their effective masses by [75,76]:

$$v_{th_e} = \sqrt{\frac{3k_B T}{m_e^*}} \text{ and } v_{th_h} = \sqrt{\frac{3k_B T}{m_h^*}}. \quad (3)$$

To compute the electron and hole mobilities, we have employed the deformation potential techniques [77] along with the acoustic phonon-limited approach. To estimate the phonon's limited mobility, we followed Bardeen–Shockley's approach [78], which says that the atomic displacement associated with a long wavelength acoustic phonon causes crystal deformation and significantly shifts the electronic energy dispersion. This change in the energy band edge with the differential displacement is characterized through the electron–phonon coupling Hamiltonian (H_{el-ph}) as:

$$H_{el-ph} = E_{dp}\nabla\cdot\vec{u}\left(\vec{r},t\right), \tag{4}$$

where E_{dp} is the deformation potential and $\vec{u}\left(\vec{r},t\right)$ is the displacement at the spatial coordinate $\vec{r}$ and time t. Further, van de Walle [79] suggested that the electron–phonon coupling Hamiltonian (H_{el-ph}) can be simplified to

$$\partial E\left(k\right) = E_{dp}\frac{\partial V}{V_0}, \tag{5}$$

where $\partial E(k)$ is the induced band edge shift due to the acoustic phonon and $\partial V/V_0$ is the fractional change in the unit cell volume due to the strain implication. After getting the value of the deformation potential using Kawaji theory [80], we can formulate the phonon-limited mobility (μ_{2D}) because of the interaction of the charge carriers with low acoustic phonons as [81]:

$$\mu_{2D} = \frac{e\hbar^3 C}{k_B T m_e^* m_d E_{dp}^2}, \tag{6}$$

where C denotes the elastic constant of a 2D material and $m_d = \sqrt{m_x^* m_y^*}$ is the geometric mean of the effective masses. The elastic constant C can be derived by knowing the interatomic force constant, calculated applying a uniaxial strain δ in the direction of lattice vector a:

$$C = \frac{\partial^2 E}{\partial^2 \delta}\frac{1}{A_0}, \tag{7}$$

where A_0 is the surface area of the unit cell.The deformation potential E_{dp} can be calculated using a band edge variation formulation $E_{dp} = \partial E_{edge}/\partial\delta$, where E_{edge} is the valence and conduction band edge, and E_{dp} is computed by imposing a compressive and tensile strain δ to the unit cell. After substituting the values of E_{dp}, elastic constant C, and average effective mass m_d, we calculate the mobility of the charge carriers (for electrons and holes).

To calculate the charge transfer and use it in the solar cell, it is required to know the electron affinity and work function of monolayer Ge_2Se_2. The electron affinity is calculated as $E_A = E_{Vac} - E_{LUMO}$, where E_A is the electron affinity, E_{Vac} is the vacuum energy level, E_{LUMO} is the LUMO energy level. The ionization potential is calculated as IP = $E_{Vac} - E_{HOMO}$, where IP, E_{Vac}, and E_{HOMO} are ionization potential, vacuum energy level, and HOMO energy level, respectively. The electron affinity at a semiconductor surface is defined as the energy needed to carry an electron from the vacuum to the bottom of the conduction band. Similarly, the work function is defined as the minimum energy required by an electron of the material to escape into the vacuum [82,83]. E_A can be calculated using DFT as the energy difference between the vacuum level (E_{Vac}) and the Kohn–Sham (KS) eigenvalues relative to the bottom of the conduction band. Along with the DFT-derived parameters, some excited state eigenfunctions in terms of absorption coefficient and dielectric constant are also required to simulate solar cell-based devices. An optimum way of extracting these optical parameters from ground-state eigenvalues is described below.

Extraction of optical properties

To explore the optical properties, including dielectric constant, refractive index, absorption constant, extinction coefficient, and susceptibility for monolayer Ge_2Se_2, we employed the non-equilibrium Green's function (NEGF) and the Kubo–Greenwood formalisms [84] as described in the Synopsys-ATK [85]. A double zeta-polarized (DZDP) basis set has been used with a localized pseudo atomic orbital to calculate optical properties and characterize the valence electrons of the constituent atoms. To maintain high accuracy, a large plane-wave mesh cutoff of 120 Ry is considered throughout the calculations. We computed the optical parameters within the range of 0–30 eV. They stem from the dielectric function (using the Kramers–Kronig relations [86]), further estimated through the susceptibility tensors. The susceptibility tensors and complex dielectric functions are related as:

$$\chi_{ij}\left(\omega\right) = \frac{e^2}{\hbar m_e^2 V}\sum_{nm\mathbf{k}}\frac{f_{m\mathbf{k}} - f_{n\mathbf{k}}}{\omega_{nm}^2\left(\mathbf{k}\right)\left[\omega_{nm}\left(\mathbf{k}\right) - \omega - i\Gamma/\hbar\right]}p_{nm}^i\left(\mathbf{k}\right)p_{mn}^j\left(\mathbf{k}\right), \tag{8}$$

where $p_{nm}^i\left(\mathbf{k}\right) = \left\langle n\mathbf{k}\middle|\mathbf{p}^i\middle|m\mathbf{k}\right\rangle$ is the i-th component (labeling electrons) of the momentum operator between states n and m, m_e and e are the electron mass and charge, respectively, V is the

volume, Γ the energy broadening, and $\hbar\omega_{nm} = E_n - E_m$ and $f_{n\mathbf{k}}$ is the Fermi function (evaluated at the energy $E_n(\mathbf{k})$).

The response coefficients, that is, the relative dielectric permittivity (ε_r), the polarizability (α), and the optical conductivity (σ), are related to the susceptibility as:

$$\varepsilon_{r,ij}(\omega) = \left(1 + \chi_{ij}(\omega)\right), \tag{9}$$

$$\alpha_{ij}(\omega) = V\varepsilon_0\chi_{ij}(\omega), \tag{10}$$

$$\sigma_{ij}(\omega) = -i\omega\varepsilon_0\chi_{ij}(\omega), \tag{11}$$

with $i,j \in \{1,2,3\}$. Solving and separating Equation 9 for the imaginary part of dielectric function, we can calculate the refractive index and extinction coefficient as

$$\varepsilon_2(\omega) = \frac{2e^2\pi}{\Omega\varepsilon_0}\sum_{k,v,c}\left|\left\langle\Psi_k^c\left|\mathbf{u}\cdot\mathbf{r}\right|\Psi_k^v\right\rangle\right|^2\delta\left[E_k^c - E_k^v - E\right]. \tag{12}$$

Here, $\left|\Psi_k^c\right\rangle$ and $\left|\Psi_k^v\right\rangle$ are the conduction and valence band Bloch states with energies E_k^c and E_k^v, respectively, **r** is the position of the electron, and **u** is the polarization of light. *e* is the electronic charge, and Ω is the volume. Via the well-known relationship between relative permittivity and refractive index $n = \eta + i\kappa = \sqrt{\varepsilon_r}$, we finally get the following relationships for the refractive index and the absorption coefficient.

Refractive index/optical density:

$$\eta(\omega) = \left[\sqrt{\varepsilon_1^2(\omega) + \varepsilon_2^2(\omega)} + \frac{\varepsilon_2(\omega)}{2}\right]^{1/2} \tag{13}$$

Extinction coefficient:

$$\kappa(\omega) = \left[\sqrt{\varepsilon_1^2(\omega) + \varepsilon_2^2(\omega)} - \frac{\varepsilon_2(\omega)}{2}\right]^{1/2} \tag{14}$$

Absorption coefficient:

$$\alpha(\omega) = \sqrt{2\pi}\left[\sqrt{\varepsilon_1^2(\omega) + \varepsilon_2^2(\omega)} - \varepsilon_1(\omega)\right]^{1/2} \tag{15}$$

Device modeling

To investigate the performance of the proposed solar cell, we performed a numerical simulation using SCAPS-1D, which solves the fundamental semiconductor equations such as drift–diffusion, Poisson's equation, and continuity equations as:

$$\frac{\partial}{\partial x}\left(\varepsilon_0\varepsilon_r\frac{\partial\phi}{\partial x}\right) = -q\left(p - n + N_D^+ - N_A^- + \frac{\rho_{\text{def}}}{q}\right), \tag{16}$$

$$-\frac{\partial J_n}{\partial x} - U_n + G_n = \frac{\partial n}{\partial t}, \tag{17}$$

and

$$-\frac{\partial J_p}{\partial x} - U_n + G_n = \frac{\partial n}{\partial t}, \tag{18}$$

where $J_n = -\frac{\mu_n n}{q}\frac{\partial E_{\text{F}_n}}{\partial x}$ and $J_p = -\frac{\mu_p p}{q}\frac{\partial E_{\text{F}_p}}{\partial x}$ are the electron and hole current densities at the Fermi levels $E_{\text{F}n}$ and $E_{\text{F}p}$, respectively. ε_0, ε_r, ϕ, q, n, and p denote the absolute and relative permittivity, the electrostatic potential, the electronic charge, and the electron and hole concentrations, respectively. The charge carrier mobilities, generation, and recombination rates for electrons and holes are represented by μ_n, G_n, U_n, μ_p, G_p, U_p, respectively. All these parameters are functions of the position coordinate *x*.

During the simulation of the proposed device, it is assumed that the reflection of the top surface is zero. In contrast, the reflection from the back surface is considered as 100%, so the all incident photons have greater energy than the bandgap of the materials and can contribute to generating charge carriers. The generated charge carrier mobility of the chosen material assists in delivering it up to the contacts.

Conclusion

This contribution investigates the electronic and optical properties of monolayer Ge_2Se_2 using DFT. The structure of the monolayer is properly optimized and relaxed for its lowest energy state. Tough threshold criteria have been chosen to maintain high precision in the calculation, along with a hybrid functional for modeling the exchange–correlation interactions. The non-imaginary frequencies in the phonon spectra confirm the stable geometry of the investigated structure. The electronic properties of the monolayer have been investigated in detail in terms of energy band diagram, effective masses of the charge carriers, mobility of electrons and holes at room temperature,

the total density of states along with effective densities in conduction and valence band, electron affinity, and ionization potentials. In addition, the optical behavior of monolayer Ge_2Se_2 has been discussed through exhaustive calculations of the material's absorption coefficient, dielectric constants, refractive index, and extinction coefficient. The optimum bandgap (1.2 eV), high carrier mobility, and promising optical characteristics of monolayer Ge_2Se_2 further led us to investigate the application of the investigated structure. To show the application of monolayer Ge_2Se_2, a perovskite solar cell has been proposed using monolayer Ge_2Se_2 as HTL. The optimal performance was determined under AM1.5G spectrum illumination. To obtain the optimum device performance, first, the ETL thickness has been varied from 10 to 100 nm, where it is found that above 20 nm, the device performance starts to diminish. Further keeping the ETL thickness at 20 nm, the absorber thickness has been tuned from 1 to 10 µm. The simulation results show an optimal device performance at 2 µm absorber thickness. Keeping the thickness of ETL and absorber layer at 20 nm and 2 µm, respectively, the HTL thickness has been changed from 1 to 10 nm. As the thickness increases, the device performance diminishes because of recombination of charge carriers in the HTL. Thus, the device exhibits optimal performance at layer thicknesses of ETL, absorber, and HTL at 20 nm, 2 µm, and 1 nm, respectively. The simulation results indicate that the proposed solar cell outperforms in terms of power conversion efficiency (around 28%) and fill factor (≈87%). In addition to the proposed solar cell, the excellent optoelectronic characteristics of the investigated monolayer Ge_2Se_2 make it a potential candidate for other photo devices. This study may also be helpful in the search for excelling materials regarding prospective applications in photo devices.

Acknowledgements

The authors would like to thank Dr. Marc Burgelman and his team from Gent University for providing the SCAPS simulator.

Funding

Anup Shrivastava acknowledges the Ministry of Education (Govt. of India) for providing financial support. Sanjai Singh acknowledges the Centralised Computation Facility, IIIT-Allahabad, for providing computational resources.

Author Contributions

Anup Shrivastava: conceptualization; formal analysis; investigation; methodology; writing – original draft. Shivani Saini: methodology; software; writing – original draft. Dolly Kumari: methodology; software. Sanjai Singh: resources; supervision; writing – review & editing. Jost Adam: project administration; supervision; validation; visualization; writing – review & editing.

ORCID® iDs

Anup Shrivastava - https://orcid.org/0000-0003-1601-5947
Shivani Saini - https://orcid.org/0000-0003-2290-8872
Dolly Kumari - https://orcid.org/0000-0003-4823-4802
Sanjai Singh - https://orcid.org/0000-0002-1783-8729
Jost Adam - https://orcid.org/0000-0001-7177-3252

Data Availability Statement

All data that supports the findings of this study is available in the published article and/or the supporting information to this article.

References

1. Noel, N. K.; Stranks, S. D.; Abate, A.; Wehrenfennig, C.; Guarnera, S.; Haghighirad, A.-A.; Sadhanala, A.; Eperon, G. E.; Pathak, S. K.; Johnston, M. B.; Petrozza, A.; Herz, L. M.; Snaith, H. J. *Energy Environ. Sci.* **2014,** *7,* 3061–3068. doi:10.1039/c4ee01076k
2. Miah, M. H.; Khandaker, M. U.; Rahman, M. B.; Nur-E-Alam, M.; Islam, M. A. *RSC Adv.* **2024,** *14,* 15876–15906. doi:10.1039/d4ra01640h
3. Salhi, B.; Wudil, Y. S.; Hossain, M. K.; Al-Ahmed, A.; Al-Sulaiman, F. A. *Renewable Sustainable Energy Rev.* **2018,** *90,* 210–222. doi:10.1016/j.rser.2018.03.058
4. Helal Miah, M.; Bulu Rahman, M.; Khatun, F.; Khandaker, M. U.; Wan Muhammad Hatta, S. F.; Soin, N. B.; Islam, M. A. *Optik (Munich, Ger.)* **2023,** *281,* 170819. doi:10.1016/j.ijleo.2023.170819
5. Kumar, V.; Kathiravan, A.; Jhonsi, M. A. *Nano Energy* **2024,** *125,* 109523. doi:10.1016/j.nanoen.2024.109523
6. Berhe, T. A.; Su, W.-N.; Chen, C.-H.; Pan, C.-J.; Cheng, J.-H.; Chen, H.-M.; Tsai, M.-C.; Chen, L.-Y.; Dubale, A. A.; Hwang, B.-J. *Energy Environ. Sci.* **2016,** *9,* 323–356. doi:10.1039/c5ee02733k
7. Di Carlo, A.; Agresti, A.; Brunetti, F.; Pescetelli, S. *JPhys Energy* **2020,** *2,* 031003. doi:10.1088/2515-7655/ab9eab
8. Miao, S.; Liu, T.; Du, Y.; Zhou, X.; Gao, J.; Xie, Y.; Shen, F.; Liu, Y.; Cho, Y. *Nanomaterials* **2022,** *12,* 2100. doi:10.3390/nano12122100
9. Zhang, H. *ACS Nano* **2015,** *9,* 9451–9469. doi:10.1021/acsnano.5b05040
10. Kumar, S.; Taunk, M. *Mater. Today Phys.* **2024,** *46,* 101483. doi:10.1016/j.mtphys.2024.101483
11. Gupta, A.; Sakthivel, T.; Seal, S. *Prog. Mater. Sci.* **2015,** *73,* 44–126. doi:10.1016/j.pmatsci.2015.02.002
12. Zhou, D.; Zhou, T.; Tian, Y.; Zhu, X.; Tu, Y. *J. Nanomater.* **2018,** *2018,* 8148072. doi:10.1155/2018/8148072
13. Ciambelli, P.; La Guardia, G.; Vitale, L. Nanotechnology for green materials and processes. In *Studies in Surface Science and Catalysis;* Basile, A.; Centi, G.; Falco, M. D.; Iaquaniello, G., Eds.; Elsevier: Amsterdam, Netherlands, 2020; Vol. 179, pp 97–116. doi:10.1016/b978-0-444-64337-7.00007-0
14. Shao, S.; Loi, M. A. *Adv. Mater. Interfaces* **2020,** *7,* 1901469. doi:10.1002/admi.201901469
15. Zhang, L.; Liu, T.; Liu, L.; Hu, M.; Yang, Y.; Mei, A.; Han, H. *J. Mater. Chem. A* **2015,** *3,* 9165–9170. doi:10.1039/c4ta04647a
16. Wang, K.-C.; Jeng, J.-Y.; Shen, P.-S.; Chang, Y.-C.; Diau, E. W.-G.; Tsai, C.-H.; Chao, T.-Y.; Hsu, H.-C.; Lin, P.-Y.; Chen, P.; Guo, T.-F.; Wen, T.-C. *Sci. Rep.* **2014,** *4,* 4756. doi:10.1038/srep04756
17. Hima, A.; Lakhdar, N. *Opt. Mater. (Amsterdam, Neth.)* **2020,** *99,* 109607. doi:10.1016/j.optmat.2019.109607

18. Kukreti, S.; Gupta, G. K.; Dixit, A. *Sol. Energy* **2021,** *225,* 802–813. doi:10.1016/j.solener.2021.07.071
19. Kohnehpoushi, S.; Nazari, P.; Nejand, B. A.; Eskandari, M. *Nanotechnology* **2018,** *29,* 205201. doi:10.1088/1361-6528/aab1d4
20. Kumar Singh, M.; V. Shinde, P.; Singh, P.; Kumar Tyagi, P. Two-Dimensional Materials for Advanced Solar Cells. In *Solar Cells - Theory, Materials and Recent Advances;* Elseman, A., Ed.; IntechOpen: London, United Kingdom, 2021. doi:10.5772/intechopen.94114
21. Bati, A. S. R.; Batmunkh, M.; Shapter, J. G. *Adv. Energy Mater.* **2020,** *10,* 1902253. doi:10.1002/aenm.201902253
22. Ross, J. S.; Klement, P.; Jones, A. M.; Ghimire, N. J.; Yan, J.; Mandrus, D. G.; Taniguchi, T.; Watanabe, K.; Kitamura, K.; Yao, W.; Cobden, D. H.; Xu, X. *Nat. Nanotechnol.* **2014,** *9,* 268–272. doi:10.1038/nnano.2014.26
23. Wang, Q. H.; Kalantar-Zadeh, K.; Kis, A.; Coleman, J. N.; Strano, M. S. *Nat. Nanotechnol.* **2012,** *7,* 699–712. doi:10.1038/nnano.2012.193
24. Li, H.; Shi, Y.; Chiu, M.-H.; Li, L.-J. *Nano Energy* **2015,** *18,* 293–305. doi:10.1016/j.nanoen.2015.10.023
25. Bernardi, M.; Palummo, M.; Grossman, J. C. *Nano Lett.* **2013,** *13,* 3664–3670. doi:10.1021/nl401544y
26. Yin, G.; Zhao, H.; Feng, J.; Sun, J.; Yan, J.; Liu, Z.; Lin, S.; Liu, S. F. *J. Mater. Chem. A* **2018,** *6,* 9132–9138. doi:10.1039/c8ta01143e
27. Zhao, X.; Liu, S.; Zhang, H.; Chang, S.-Y.; Huang, W.; Zhu, B.; Shen, Y.; Shen, C.; Wang, D.; Yang, Y.; Wang, M. *Adv. Funct. Mater.* **2019,** *29,* 1805168. doi:10.1002/adfm.201805168
28. Mukherjee, B.; Cai, Y.; Tan, H. R.; Feng, Y. P.; Tok, E. S.; Sow, C. H. *ACS Appl. Mater. Interfaces* **2013,** *5,* 9594–9604. doi:10.1021/am402550s
29. Chang, K.; Parkin, S. S. P. *APL Mater.* **2019,** *7,* 041102. doi:10.1063/1.5091546
30. An, B.; Ma, Y.; Zhang, G.; You, C.; Zhang, Y. *RSC Adv.* **2020,** *10,* 42157–42163. doi:10.1039/d0ra08360g
31. Lin, Y.-T.; Shi, J.-B.; Chen, Y.-C.; Chen, C.-J.; Wu, P.-F. *Nanoscale Res. Lett.* **2009,** *4,* 694–698. doi:10.1007/s11671-009-9299-5
32. Zhou, X.; Zhang, Q.; Gan, L.; Li, H.; Xiong, J.; Zhai, T. *Adv. Sci.* **2016,** *3,* 1600177. doi:10.1002/advs.201600177
33. Xia, J.; Li, X.-Z.; Huang, X.; Mao, N.; Zhu, D.-D.; Wang, L.; Xu, H.; Meng, X.-M. *Nanoscale* **2016,** *8,* 2063–2070. doi:10.1039/c5nr07675g
34. Huang, Y.; Ling, C.; Liu, H.; Wang, S.; Geng, B. *J. Phys. Chem. C* **2014,** *118,* 9251–9260. doi:10.1021/jp5013158
35. Wang, X.; Liu, B.; Wang, Q.; Song, W.; Hou, X.; Chen, D.; Cheng, Y.-b.; Shen, G. *Adv. Mater. (Weinheim, Ger.)* **2013,** *25,* 1479–1486. doi:10.1002/adma.201204063
36. Mukherjee, B.; Tok, E. S.; Sow, C. H. *J. Appl. Phys.* **2013,** *114,* 134302. doi:10.1063/1.4823779
37. Mukherjee, B.; Hu, Z.; Zheng, M.; Cai, Y.; Feng, Y. P.; Tok, E. S.; Sow, C. H. *J. Mater. Chem.* **2012,** *22,* 24882–24888. doi:10.1039/c2jm35006h
38. Properzi, L.; Di Cicco, A.; Nataf, L.; Baudelet, F.; Irifune, T. *Sci. Rep.* **2015,** *5,* 10188. doi:10.1038/srep10188
39. Zang, H.; Routh, P. K.; Huang, Y.; Chen, J.-S.; Sutter, E.; Sutter, P.; Cotlet, M. *ACS Nano* **2016,** *10,* 4790–4796. doi:10.1021/acsnano.6b01538
40. Zhou, T.; Pang, W. K.; Zhang, C.; Yang, J.; Chen, Z.; Liu, H. K.; Guo, Z. *ACS Nano* **2014,** *8,* 8323–8333. doi:10.1021/nn503582c
41. Saini, S.; Shrivastava, A.; Singh, S. *Phys. E (Amsterdam, Neth.)* **2022,** *138,* 115060. doi:10.1016/j.physe.2021.115060
42. Seixas, L. *J. Appl. Phys.* **2020,** *128,* 045115. doi:10.1063/5.0012427
43. Kong, B. D.; Paul, S.; Nardelli, M. B.; Kim, K. W. *Phys. Rev. B: Condens. Matter Mater. Phys.* **2009,** *80,* 033406. doi:10.1103/physrevb.80.033406
44. Qin, G.; Yan, Q.-B.; Qin, Z.; Yue, S.-Y.; Hu, M.; Su, G. *Phys. Chem. Chem. Phys.* **2015,** *17,* 4854–4858. doi:10.1039/c4cp04858j
45. Peng, B.; Zhang, H.; Shao, H.; Xu, Y.; Zhang, X.; Zhu, H. *Sci. Rep.* **2016,** *6,* 20225. doi:10.1038/srep20225
46. Haastrup, S.; Strange, M.; Pandey, M.; Deilmann, T.; Schmidt, P. S.; Hinsche, N. F.; Gjerding, M. N.; Torelli, D.; Larsen, P. M.; Riis-Jensen, A. C.; Gath, J.; Jacobsen, K. W.; Jørgen Mortensen, J.; Olsen, T.; Thygesen, K. S. *2D Mater.* **2018,** *5,* 042002. doi:10.1088/2053-1583/aacfc1
47. Gjerding, M. N.; Taghizadeh, A.; Rasmussen, A.; Ali, S.; Bertoldo, F.; Deilmann, T.; Knøsgaard, N. R.; Kruse, M.; Larsen, A. H.; Manti, S.; Pedersen, T. G.; Petralanda, U.; Skovhus, T.; Svendsen, M. K.; Mortensen, J. J.; Olsen, T.; Thygesen, K. S. *2D Mater.* **2021,** *8,* 044002. doi:10.1088/2053-1583/ac1059
48. Chattopadhyay, S.; Kokenyesi, R. S.; Hong, M. J.; Watts, C. L.; Labram, J. G. *J. Mater. Chem. C* **2020,** *8,* 10761–10766. doi:10.1039/d0tc00328j
49. Kahn, A. *Mater. Horiz.* **2016,** *3,* 7–10. doi:10.1039/c5mh00160a
50. Singh, D.; Gupta, S. K.; Sonvane, Y.; Lukačević, I. *J. Mater. Chem. C* **2016,** *4,* 6386–6390. doi:10.1039/c6tc01913g
51. Patel, P. K. *Sci. Rep.* **2021,** *11,* 3082. doi:10.1038/s41598-021-82817-w
52. Urieta-Mora, J.; García-Benito, I.; Molina-Ontoria, A.; Martín, N. *Chem. Soc. Rev.* **2018,** *47,* 8541–8571. doi:10.1039/c8cs00262b
53. Kim, G.-W.; Choi, H.; Kim, M.; Lee, J.; Son, S. Y.; Park, T. *Adv. Energy Mater.* **2020,** *10,* 1903403. doi:10.1002/aenm.201903403
54. Wang, D.; Elumalai, N. K.; Mahmud, M. A.; Yi, H.; Upama, M. B.; Lee Chin, R. A.; Conibeer, G.; Xu, C.; Haque, F.; Duan, L.; Uddin, A. *Synth. Met.* **2018,** *246,* 195–203. doi:10.1016/j.synthmet.2018.10.012
55. Bag, A.; Radhakrishnan, R.; Nekovei, R.; Jeyakumar, R. *Sol. Energy* **2020,** *196,* 177–182. doi:10.1016/j.solener.2019.12.014
56. Kim, G.-W.; Shinde, D. V.; Park, T. *RSC Adv.* **2015,** *5,* 99356–99360. doi:10.1039/c5ra18648j
57. Jeyakumar, R.; Bag, A.; Nekovei, R.; Radhakrishnan, R. *J. Electron. Mater.* **2020,** *49,* 3533–3539. doi:10.1007/s11664-020-08041-w
58. Kumari, D.; Pandey, S. K. *J. Opt. Soc. Am. B* **2022,** *39,* 756–763. doi:10.1364/josab.443938
59. Abdelaziz, W.; Shaker, A.; Abouelatta, M.; Zekry, A. *Opt. Mater. (Amsterdam, Neth.)* **2019,** *91,* 239–245. doi:10.1016/j.optmat.2019.03.023
60. Bhatt, S.; Shukla, R.; Pathak, C.; Pandey, S. K. *IEEE Trans. Electron Devices* **2020,** *67,* 2837–2843. doi:10.1109/ted.2020.2996570
61. Zhang, X.; Turiansky, M. E.; Van de Walle, C. G. *J. Phys. Chem. C* **2020,** *124,* 6022–6027. doi:10.1021/acs.jpcc.0c01324
62. Ahmed, S.; Jannat, F.; Khan, M. A. K.; Alim, M. A. *Optik (Munich, Ger.)* **2021,** *225,* 165765. doi:10.1016/j.ijleo.2020.165765
63. Nejand, B. A.; Ahmadi, V.; Gharibzadeh, S.; Shahverdi, H. R. *ChemSusChem* **2016,** *9,* 302–313. doi:10.1002/cssc.201501273
64. Kaity, A.; Shubham; Singh, S.; Pandey, S. K. *Superlattices Microstruct.* **2021,** *156,* 106972. doi:10.1016/j.spmi.2021.106972

65. Giannozzi, P.; Andreussi, O.; Brumme, T.; Bunau, O.; Buongiorno Nardelli, M.; Calandra, M.; Car, R.; Cavazzoni, C.; Ceresoli, D.; Cococcioni, M.; Colonna, N.; Carnimeo, I.; Dal Corso, A.; de Gironcoli, S.; Delugas, P.; DiStasio, R. A., Jr.; Ferretti, A.; Floris, A.; Fratesi, G.; Fugallo, G.; Gebauer, R.; Gerstmann, U.; Giustino, F.; Gorni, T.; Jia, J.; Kawamura, M.; Ko, H.-Y.; Kokalj, A.; Küçükbenli, E.; Lazzeri, M.; Marsili, M.; Marzari, N.; Mauri, F.; Nguyen, N. L.; Nguyen, H.-V.; Otero-de-la-Roza, A.; Paulatto, L.; Poncé, S.; Rocca, D.; Sabatini, R.; Santra, B.; Schlipf, M.; Seitsonen, A. P.; Smogunov, A.; Timrov, I.; Thonhauser, T.; Umari, P.; Vast, N.; Wu, X.; Baroni, S. *J. Phys.: Condens. Matter* **2017,** *29,* 465901. doi:10.1088/1361-648x/aa8f79
66. Giannozzi, P.; Baroni, S.; Bonini, N.; Calandra, M.; Car, R.; Cavazzoni, C.; Ceresoli, D.; Chiarotti, G. L.; Cococcioni, M.; Dabo, I.; Dal Corso, A.; de Gironcoli, S.; Fabris, S.; Fratesi, G.; Gebauer, R.; Gerstmann, U.; Gougoussis, C.; Kokalj, A.; Lazzeri, M.; Martin-Samos, L.; Marzari, N.; Mauri, F.; Mazzarello, R.; Paolini, S.; Pasquarello, A.; Paulatto, L.; Sbraccia, C.; Scandolo, S.; Sclauzero, G.; Seitsonen, A. P.; Smogunov, A.; Umari, P.; Wentzcovitch, R. M. *J. Phys.: Condens. Matter* **2009,** *21,* 395502. doi:10.1088/0953-8984/21/39/395502
67. Zhao, G. L.; Bagayoko, D.; Williams, T. D. *Phys. Rev. B: Condens. Matter Mater. Phys.* **1999,** *60,* 1563–1572. doi:10.1103/physrevb.60.1563
68. Grimme, S. *J. Comput. Chem.* **2006,** *27,* 1787–1799. doi:10.1002/jcc.20495
69. Perdew, J. P.; Burke, K.; Ernzerhof, M. *Phys. Rev. Lett.* **1996,** *77,* 3865–3868. doi:10.1103/physrevlett.77.3865
70. Heyd, J.; Scuseria, G. E.; Ernzerhof, M. *J. Chem. Phys.* **2003,** *118,* 8207–8215. doi:10.1063/1.1564060
71. Troullier, N.; Martins, J. L. *Phys. Rev. B: Condens. Matter Mater. Phys.* **1991,** *43,* 1993–2006. doi:10.1103/physrevb.43.1993
72. Monkhorst, H. J.; Pack, J. D. *Phys. Rev. B: Condens. Matter Mater. Phys.* **1976,** *13,* 5188–5192. doi:10.1103/physrevb.13.5188
73. Tadano, T.; Gohda, Y.; Tsuneyuki, S. *J. Phys.: Condens. Matter* **2014,** *26,* 225402. doi:10.1088/0953-8984/26/22/225402
74. Green, M. A. *J. Appl. Phys.* **1990,** *67,* 2944–2954. doi:10.1063/1.345414
75. Chaurasiya, R.; Gupta, G. K.; Dixit, A. *Sol. Energy Mater. Sol. Cells* **2019,** *201,* 110076. doi:10.1016/j.solmat.2019.110076
76. Cozza, D.; Ruiz, C. M.; Duche, D.; Simon, J. J.; Escoubas, L. *IEEE J. Photovoltaics* **2016,** *6,* 1292–1297. doi:10.1109/jphotov.2016.2576678
77. Shuai, Z.; Wang, L.; Song, C. *Deformation Potential Theory;* SpringerBriefs in Molecular Science; Springer Berlin: Berlin, Germany, 2012; pp 67–88. doi:10.1007/978-3-642-25076-7_4
78. Bardeen, J.; Shockley, W. *Phys. Rev.* **1950,** *80,* 72–80. doi:10.1103/physrev.80.72
79. Van de Walle, C. G. *Phys. Rev. B: Condens. Matter Mater. Phys.* **1989,** *39,* 1871–1883. doi:10.1103/physrevb.39.1871
80. Kawaji, S. *J. Phys. Soc. Jpn.* **1969,** *27,* 906–908. doi:10.1143/jpsj.27.906
81. Sharma, G.; Datta, S.; Ghosh, P. *J. Electron. Mater.* **2021,** *50,* 1644–1654. doi:10.1007/s11664-020-08479-y
82. Khan, F.; Din, H. U.; Khan, S. A.; Rehman, G.; Bilal, M.; Nguyen, C. V.; Ahmad, I.; Gan, L.-Y.; Amin, B. *J. Phys. Chem. Solids* **2019,** *126,* 304–309. doi:10.1016/j.jpcs.2018.11.021
83. Madas, S.; Mishra, S. K.; Kahaly, S.; Kahaly, M. U. *Sci. Rep.* **2019,** *9,* 10307. doi:10.1038/s41598-019-44823-x
84. Sipe, J. E.; Ghahramani, E. *Phys. Rev. B: Condens. Matter Mater. Phys.* **1993,** *48,* 11705–11722. doi:10.1103/physrevb.48.11705
85. Smidstrup, S.; Markussen, T.; Vancraeyveld, P.; Wellendorff, J.; Schneider, J.; Gunst, T.; Verstichel, B.; Stradi, D.; Khomyakov, P. A.; Vej-Hansen, U. G.; Lee, M.-E.; Chill, S. T.; Rasmussen, F.; Penazzi, G.; Corsetti, F.; Ojanperä, A.; Jensen, K.; Palsgaard, M. L. N.; Martinez, U.; Blom, A.; Brandbyge, M.; Stokbro, K. *J. Phys.: Condens. Matter* **2020,** *32,* 015901. doi:10.1088/1361-648x/ab4007
86. Probert, M. *Contemp. Phys.* **2020,** *61,* 312. doi:10.1080/00107514.2021.1890832

License and Terms

BEILSTEIN JOURNAL OF NANOTECHNOLOGY

Strain-induced bandgap engineering in 2D ψ-graphene materials: a first-principles study

Kamal Kumar[1], Nora H. de Leeuw[2,3], Jost Adam[*4,5] and Abhishek Kumar Mishra[*1]

Full Research Paper

Open Access

Address:
[1]Department of Physics, Applied Science Cluster, School of Advanced Engineering, University of Petroleum and Energy Studies (UPES), Bidholi via Premnagar, Dehradun, Uttarakhand 248007, India, [2]School of Chemistry, University of Leeds, Leeds LS2 9JT, UK, [3]Department of Earth Sciences, Utrecht University, 3584 CB Utrecht, Netherlands, [4]Computational Materials and Photonics, Electrical Engineering and Computer Science (FB 16) and Institue of Physics (FB 10), University of Kassel, Wilhelmshöher Allee 71, 34121 Kassel, Germany and [5]Center for Interdisciplinary Nanostructure Science and Technology, University of Kassel, Heinrich-Plett-Straße 40, 34132 Kassel, Germany

Email:
Jost Adam[*] - jost.adam@uni-kassel.de;
Abhishek Kumar Mishra[*] - akmishra@ddn.upes.ac.in

* Corresponding author

Keywords:
2D materials; defects; DFT; graphene; ψ-graphene; strain

Beilstein J. Nanotechnol. **2024,** *15,* 1440–1452.
https://doi.org/10.3762/bjnano.15.116

Received: 22 May 2024
Accepted: 23 October 2024
Published: 20 November 2024

This article is part of the thematic issue "Smart nanomaterials in electronics and photonics".

Associate Editor: P. Ayala

Abstract

High mechanical strength, excellent thermal and electrical conductivity, and tunable properties make two-dimensional (2D) materials attractive for various applications. However, the metallic nature of these materials restricts their applications in specific domains. Strain engineering is a versatile technique to tailor the distribution of energy levels, including bandgap opening between the energy bands. ψ-Graphene is a newly predicted 2D nanosheet of carbon atoms arranged in 5,6,7-membered rings. The half and fully hydrogenated (hydrogen-functionalized) forms of ψ-graphene are called ψ-graphone and ψ-graphane. Like ψ-graphene, ψ-graphone has a zero bandgap, but ψ-graphane is a wide-bandgap semiconductor. In this study, we have applied in-plane and out-of-plane biaxial strain on pristine and hydrogenated ψ-graphene. We have obtained a bandgap opening (200 meV) in ψ-graphene at 14% in-plane strain, while ψ-graphone loses its zero-bandgap nature at very low values of applied strain (both +1% and −1%). In contrast, fully hydrogenated ψ-graphene remains unchanged under the influence of mechanical strain, preserving its initial characteristic of having a direct bandgap. This behavior offers opportunities for these materials in various vital applications in photodetectors, solar cells, LEDs, pressure and strain sensors, energy storage, and quantum computing. The mechanical strain tolerance of pristine and fully hydrogenated ψ-graphene is observed to be −17% to +17%, while for ψ-graphone, it lies within the strain span of −16% to +16%.

Introduction

Graphene is the best-known zero-bandgap two-dimensional (2D) material, consisting of a single layer of sp^2-hybridized carbon atoms arranged together in a hexagonal lattice [1]. Because of its extraordinary electrical and thermal conductivity, large surface area, and easy chemical functionalization, it provides a variety of applications in pliable displays and as strengthening material in composites [2-4]. It has also gained considerable attention among researchers for its application in hydrogen storage, owing to its good adsorption capacity and controllable storage and re-release of hydrogen at efficient temperatures [4,5]. The geometrical structures of graphene obtained from its half and full hydrogenation are called, respectively, graphone [6] and graphane [7]. Zhao et al. have reported the successful synthesis of graphone on a Ni(111) surface [8]. Their X-ray photoelectron diffraction (XPD), temperature programmed desorption (TPD), and density functional theory (DFT) study suggests that the hydrogenation of graphene with atomic hydrogen leads to the formation of graphone [8]. The full hydrogenation of graphene (graphane) was experimentally obtained by Elias et al., and their TEM and Raman spectroscopy results evidence the transition of graphene from a semimetal to an insulator after full hydrogenation [9]. After the discovery of graphene, other novel 2D materials, such as goldene [10], stanene [11], plumbene [12], antimonene [13], and arsenene [14], have been predicted and experimentally synthesized. Few of these materials are zero-bandgap, like goldene [15] and ψ-graphene [16]. The absence of bandgaps in 2D materials makes them unsuitable for conventional semiconductor applications and limits their use in photonics and optical devices [17]. Therefore, bandgap engineering (manipulation of electronic band structures (EBSs)) of these materials becomes essential to expand their utility in energy-related and optoelectronic applications [18,19]. Engineering of the electronic gap not only broadens the possible use of 2D materials but also enables them to satisfy the demand for ultramodern technologies [20]. Bandgap engineering can be achieved through different techniques like (i) doping, where the introduction of dopants or impurities modifies the EBS [21], (ii) strain engineering by inserting mechanical strain to alter the electronic properties [22,23], and (iii) defect engineering [24]. Among these techniques, strain engineering is an advantageous method because of its versatility (it can be used for a wide range of materials) [25], precise control (it can efficiently increase and decrease the bandgap according to requirements) [26], non-destructive nature (intrinsic properties of the materials can be preserved) [27], and compatibility with established technologies (the semiconductor industry can adopt it to enhance the performance of devices) [28]. Strain can be introduced in graphene using different methods, namely, by exploiting a mismatch in thermal expansion between graphene and the underlying substrate, by transferring graphene to a piezoelectric substrate, by shrinking or elongating the substrate by applying a bias voltage, or by using the tip of an atomic force microscope (AFM) to push graphene over a hole created in the substrate [29]. A wealth of literature on strain engineering of graphene and other 2D materials using different experimental techniques is available. Ni et al. synthesized graphene on a polyethylene terephthalate (PET) substrate and studied the effect of uniaxial strain through Raman spectroscopy [30]. They stretched PET in one direction and found a redshift in the D and G bands for a single graphene layer. Also, uniaxial strain of 0.8% can be introduced in graphene by stretching [30]. Conley et al. studied the effect of uniaxial tensile strain on mono- and bilayer MoS_2, where the strain was introduced in MoS_2 through a four-point bending apparatus and a transition from an optical direct bandgap to an optical indirect bandgap in MoS_2 at 1% strain was observed [31].

Gui et al. examined the EBS of graphene exposed to different planar strain patterns using both first-principles and tight-binding approaches [32]. They found that graphene maintains its zero-bandgap nature under the influence of symmetrical strain [32]. However, when it underwent asymmetrical strain, the bandgap reached 0.486 eV (on applying strain parallel to the C–C bonds) and 0.170 eV (on applying strain perpendicular to the C–C bonds) at 12.2% and 7.3% strain, respectively [32]. Kerszberg et al. have used density functional theory (DFT) calculations to investigate the modification of the electronic properties of graphene through strain engineering [33]. They found that isotropic and biaxial strains cannot open graphene's bandgap [33]. In contrast, the presence of biaxial strain and compression along zig-zag (11%) and armchair (−20%) directions can open the bandgap of graphene up to 1 eV [33]. The application of strain engineering is not restricted to tailoring the electronic properties of graphene; it can also be employed to change the electronic characteristics of novel 2D post-graphene materials [34-36]. Xu et al. found a shift from an indirect bandgap to a direct bandgap in arsenene under uniaxial strain along the zig-zag direction [37]. Mohan et al. employed DFT to study the effect of strain on the electrical band structure of a silicene monolayer and found a bandgap (335 meV) opening in silicene at 4% compressive uniaxial strain [34]. At 6% strain, a maximum bandgap of 389 meV and 379 meV was observed for uniaxial and biaxial strains, respectively. When the applied strain exceeds a threshold of 8%, the bandgap of silicene disappears [34].

In 2017, Li et al. predicted a new 2D allotrope of carbon atoms, using first-principles calculations, named ψ-graphene [16]. It is a flat sheet of 5,6,7-membered carbon rings that is dynamically and thermally stable [16,38]. It can be constructed from the

short-chain hydrocarbon *s*-indacene and has the chemical formula $C_{12}H_8$ [16]. Because of the absence of a bandgap, ψ-graphene can be used in optical detectors [39]. However, a first principles-based computational study has shown that its zero bandgap is a major challenge to its suitability in optoelectronic and electronic devices [40]. Despite being less stable than graphene, the mechanical properties of ψ-graphene are similar, and on increasing the ratio of hexagonal rings in ψ-graphene (i.e., *n*-hex-ψ-graphene), its total energy was found to be −9.23 eV/atom, which is identical to pristine graphene [16]. Another effective method to enhance the stability of ψ-graphene is edge hydrogenation, which leads to a metal-to-insulator transition, making it suitable for operating at ultrahigh speeds. ψ-Graphone and ψ-graphane are, respectively, the half and fully hydrogenated forms of ψ-graphene [41]. Like graphene, ψ-graphone possesses a zero bandgap, but ψ-graphane is an insulator with a bandgap of 4.13 eV [39]. Although a successful experimental synthesis of ψ-graphene has not yet been realized, many theoretical investigations have been carried out by different research teams to study its various potential applications in sensors, lithium-ion batteries, and hydrogen storage [16,39,42]. We have recently employed detailed density functional theory calculations with dispersion correction and on-site Coulomb interaction (DFT(D) + U) to investigate CO_2 activation on ψ-graphene and its hydrogenated forms for their application in the electrochemical conversion of CO_2 [43]. Faghihnasiri et al. have performed DFT calculations and concluded that ψ-graphene has the potential to be employed in infrared (IR) sensors, ultraviolet (UV) optomechanical sensors, and visible-light sensors [39]. Li et al. theoretically reported a maximum theoretical storage capacity of 372 $mAh{\cdot}g^{-1}$ for Li, showing its capability to be utilized as an anode material in Li-ion batteries [16]. Theoretical investigations also suggest that when ψ-graphene is decorated with transition metals like zirconium, yttrium, and titanium, it can serve as an excellent adsorbent for hydrogen storage [42,44,45]. DFT calculations have shown that the adsorption energies of hydrogen molecules over Zr-, Y-, and Ti-decorated ψ-graphene are found to lie within the standard range of −0.2 to −0.7 eV specified by the Department of Energy (DoE) [42,44,45]. However, bandgap engineering, for example, passivation, doping, or strain engineering, is crucial to modify and improve the bandgap for various electronic applications. In this study, we have investigated the electronic properties of pristine and hydrogenated ψ-graphene (i.e., ψ-graphone and ψ-graphane) under the influence of uniform biaxial mechanical strain (positive and negative).

Results and Discussion

Structural and electronic properties of 2D nanosheets without strain

We first estimated lattice parameters, bond lengths, and atomic positions of our 2D nanosheets (ψ-graphene, ψ-graphone, and ψ-graphone) by utilizing structural details available from the literature [38,39]. Subsequently, we have relaxed the nanosheets using the established computational parameters outlined in the Computational Methodology section. Table 1 summarizes the relaxed cell lattice parameters and C–C and C–H bond lengths of the three materials, which match well with earlier DFT results [38,39]. Each nanosheet has four inequivalent carbon atoms labeled C1, C2, C3, and C4, possessing unique chemical and physical attributes (Figure 1). At the junction of three *s*-indacene molecules, the C–C bond length d_1 is significantly longer than typical C–C bonds (Figure 1).

To investigate the electronic properties of these 2D nanosheets, we performed EBS and density of states (DOS) calculations (Figure 1) alongside projected orbital calculations of the different atoms to understand their contributions to the electronic states. Our calculations reveal no gap between the energy bands in both ψ-graphene and ψ-graphone (Figure 1a,b), with finite states present at the Fermi level (E_f). The dominant energy orbitals in the projected density of states (PDOS) of ψ-graphene and ψ-graphone are the outermost C 2p orbitals. In the fully hydrogenated form, that is, in ψ-graphane, we note a discernible separation of 3.78 eV between the valence and conduction bands in the EBS. This material is a direct-bandgap material

Table 1: Optimized lattice parameters (*a*, *b*), carbon–carbon bond lengths (d_1, $d_{C–C}$), carbon–hydrogen bond lengths ($d_{C–H}$), buckling heights (*h*), and bandgap energies (E_g) of ψ-graphene, ψ-graphone, and ψ-graphane 2D nanosheets.

Material		*a* (Å)	*b* (Å)	d_1 (Å)	$d_{C–C}$ (Å)	$d_{C–H}$ (Å)	*h* (Å)	E_g (eV)
ψ-graphene	our work	6.70	4.83	1.51	1.42–1.44	—	0.00	zero
	previous work [38]	6.70	4.84	1.51	1.41–1.44	—	0.00	zero
ψ-graphone	our work	6.70	4.83	1.61	1.47–1.57	1.14	1.79	zero
	previous work [39]	6.70	4.84	—	—	—	—	zero
ψ-graphane	our work	6.71	4.83	1.56	1.49–1.55	1.11	0.85	3.78
	previous work [41]	6.70	4.84	1.53	1.52–1.53	—	—	4.13

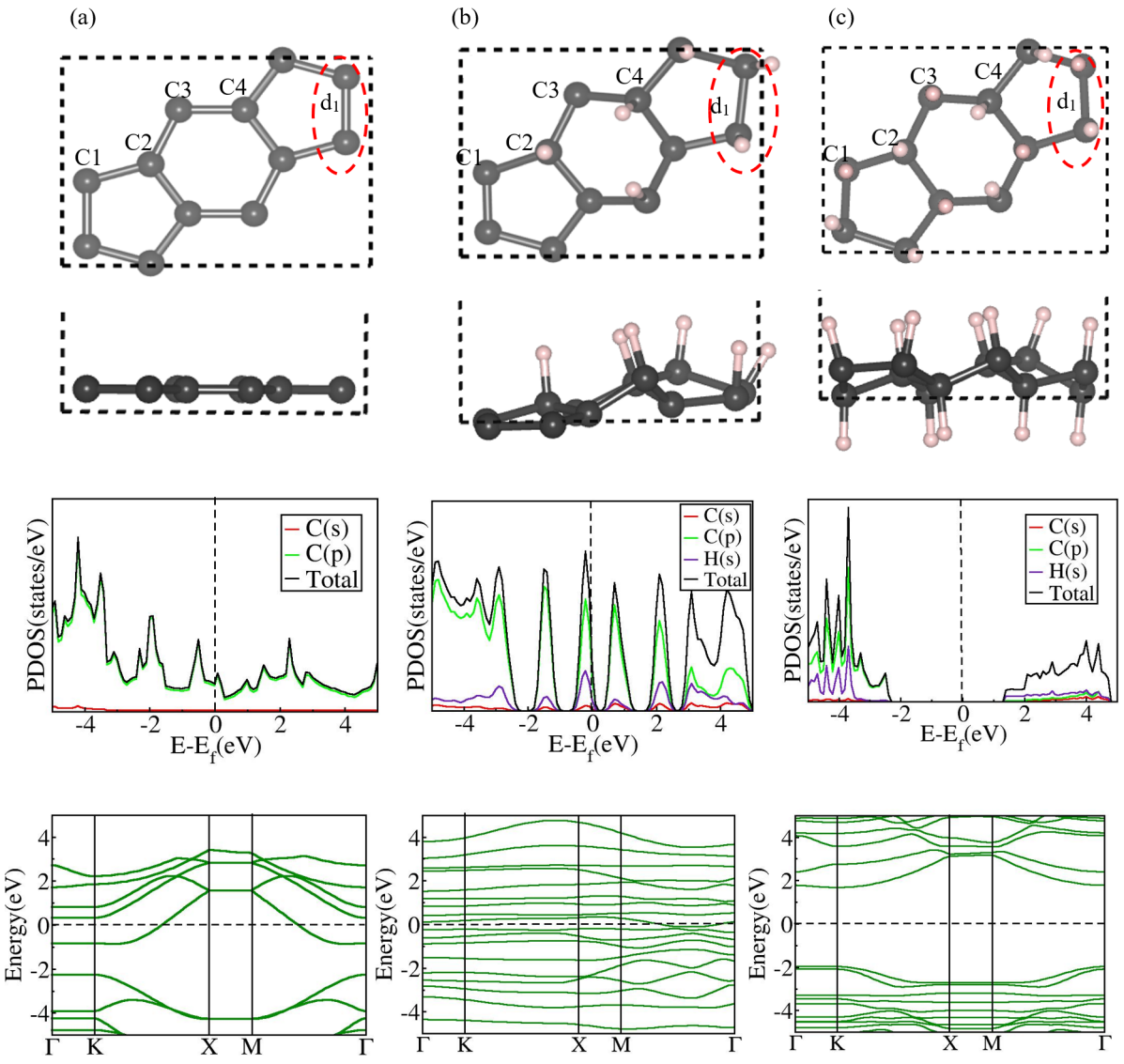

Figure 1: Top and side views of relaxed geometries, PDOS, and EBSs of (a) ψ-graphene, (b) ψ-graphone, and (c) ψ-graphane. The black dashed square boxes in the structures represent the unit cells. Black and pink balls are carbon and hydrogen atoms, respectively. Both ψ-graphene and ψ-graphone exhibit zero bandgaps, while ψ-graphane has a wide bandgap of 3.78 eV.

with the alignment of the conduction band's minima and valence band's maxima at the same k-points in the Brillouin zone (Figure 1c). We tabulate the structural parameters, bandgap, and buckling heights of these structures in Table 1. From Table 1 and Figure 1, it is clear that, while ψ-graphene is a flat 2D material, ψ-graphone and ψ-graphane are buckled sheets, and their buckling heights are 1.79 and 0.85 Å, respectively.

Structural and electronic properties of ψ-graphene with strain

We tabulate the structural parameters, buckling heights, and electronic bandgap values of all strained structures in Table 2.

Positive strain

We applied positive strain toward deliberate expansion of the structure, particularly focusing on the lattice plane, varying its value from 1% to 17% (Supporting Information File 1, Figure S1). We observed that the positive strain fails to open the bandgap in ψ-graphene (Table 2). To comprehensively analyze the impact of this positive strain on the electrical properties of ψ-graphene, we have also plotted the PDOSs and the EBSs of all the strained structures of ψ-graphene in Figure S2 and Figure S3 (Supporting Information File 1), respectively. We observed that on applying positive strain, d_1, a C–C bond length in ψ-graphene changes to 1.49 Å in all strained structures from its initial value of 1.51 Å. Concurrently, the remaining C–C bond

Table 2: Lattice parameters (a, b), C–C bond lengths (d_1, $d_{C–C}$), average C–C bond length ($d_{C–C}$(avg)), buckling height (h), and bandgap energy (E_g) of ψ-graphene on applying lattice strain.

Applied strain	Lattice parameters (Å)		d (Å)			h (Å)	E_g (eV)	Bandgap type
	a	b	d_1	$d_{C–C}$	$d_{C–C}$(avg)			
−17%	5.56	4.01	1.36	1.37–1.59	1.48	1.956	zero	—
−16%	5.63	4.06	1.34	1.32–1.53	1.42	2.232	0.700	indirect
−15%	5.69	4.11	1.35	1.32–1.53	1.42	2.182	0.400	indirect
−14%	5.76	4.15	1.36	1.32–1.52	1.42	2.132	0.200	direct
−13%	5.83	4.21	1.35	1.34–1.44	1.39	1.903	zero	—
−10%	6.03	4.35	1.27	1.34–1.33	1.34	0.007	zero	—
−7%	6.23	4.50	1.38	1.31–1.34	1.32	0.005	zero	—
−5%	6.36	4.59	1.41	1.34–1.37	1.35	0.004	zero	—
−3%	6.50	4.69	1.45	1.36–1.40	1.38	0.004	zero	—
−2%	6.57	4.74	1.47	1.38–1.41	1.40	0.004	zero	—
−1%	6.63	4.01	1.49	1.39–1.42	1.41	0.004	zero	—
0%	6.70	4.83	1.51	1.42–1.44	1.42	—	zero	—
1%	6.77	4.88	1.49	1.40–1.42	1.41	0.004	zero	—
2%	6.83	4.93	1.49	1.39–1.42	1.41	0.004	zero	—
3%	6.90	4.98	1.49	1.39–1.42	1.41	0.004	zero	—
5%	7.03	5.08	1.49	1.39–1.42	1.41	0.004	zero	—
7%	7.17	5.17	1.49	1.39–1.40	1.40	0.004	zero	—
10%	7.37	5.46	1.49	1.39–1.40	1.40	0.004	zero	—
13%	7.57	5.46	1.49	1.39–1.42	1.41	0.004	zero	—
14%	7.64	5.51	1.49	1.39–1.42	1.41	0.004	zero	—
15%	7.71	5.56	1.49	1.39–1.42	1.41	0.004	zero	—
16%	7.77	5.61	1.49	1.39–1.42	1.41	0.004	zero	—
17%	7.84	5.66	1.49	1.39–1.42	1.41	0.004	zero	—

lengths remain uniform with a mean value of 1.40–1.41 Å, as shown in Table 2. Moreover, the ψ-graphene nanosheet remains almost flat, with a buckling height of only 0.004 Å, indicating the stability of the remaining C–C bonds even under the influence of positive strain.

Negative strain

We next investigated the impact of negative strain on the structural and electronic properties of ψ-graphene (Table 2). We show structure geometries, PDOS, and EBS of different negatively strained structures in Supporting Information File 1, Figures S1, S4, and S5, respectively. Our investigation reveals that, on progressively increasing the magnitude of applied negative strain in the lattice plane, ψ-graphene maintains its conductive nature until −13%; at −14%, a bandgap of ≈0.2 eV emerges between the valence and conduction bands as shown in Figure 2. Beyond −14% negative strain, a proportional increment in the bandgap is observed, reaching its maximum value of 0.7 eV at −16% strain. On surpassing −16% strain, the bandgap suddenly disappears at −17% strain (Figure S4, Supporting Information File 1). Beyond −17% strain, a significant distortion in the lattice structure of ψ-graphene was observed, which indicates a limit on the maximum strain that the ψ-graphene nanosheet can tolerate before structural breakdown. The EBS of ψ-graphene, plotted in Figure 2b at −14%, reveals a direct transition of electrons from the valence band to the conduction band, but beyond −14% strain, no direct transition is possible, indicating the indirect nature of the bandgap of ψ-graphene at strain levels of −15% and −6% (Table 2). The bond length d_1, which was 1.51 Å in the absence of deformation, undergoes a considerable reduction under compression in the lattice plane. This bond length decreases until it reaches the lowest value of 1.27 Å at −10% strain level. The remaining C–C bond lengths fluctuate as the applied strain level increases or decreases.

It is known that the in-plane stiffness of ψ-graphene is higher than that of penta-graphene and is comparable to that of graphene [16]. Therefore, it can resist compressive strain (negative strain) in its lattice plane without experiencing much out-plane deformation or buckling. Here, we observe that ψ-graphene retains its flat structure up to −10% with negligible

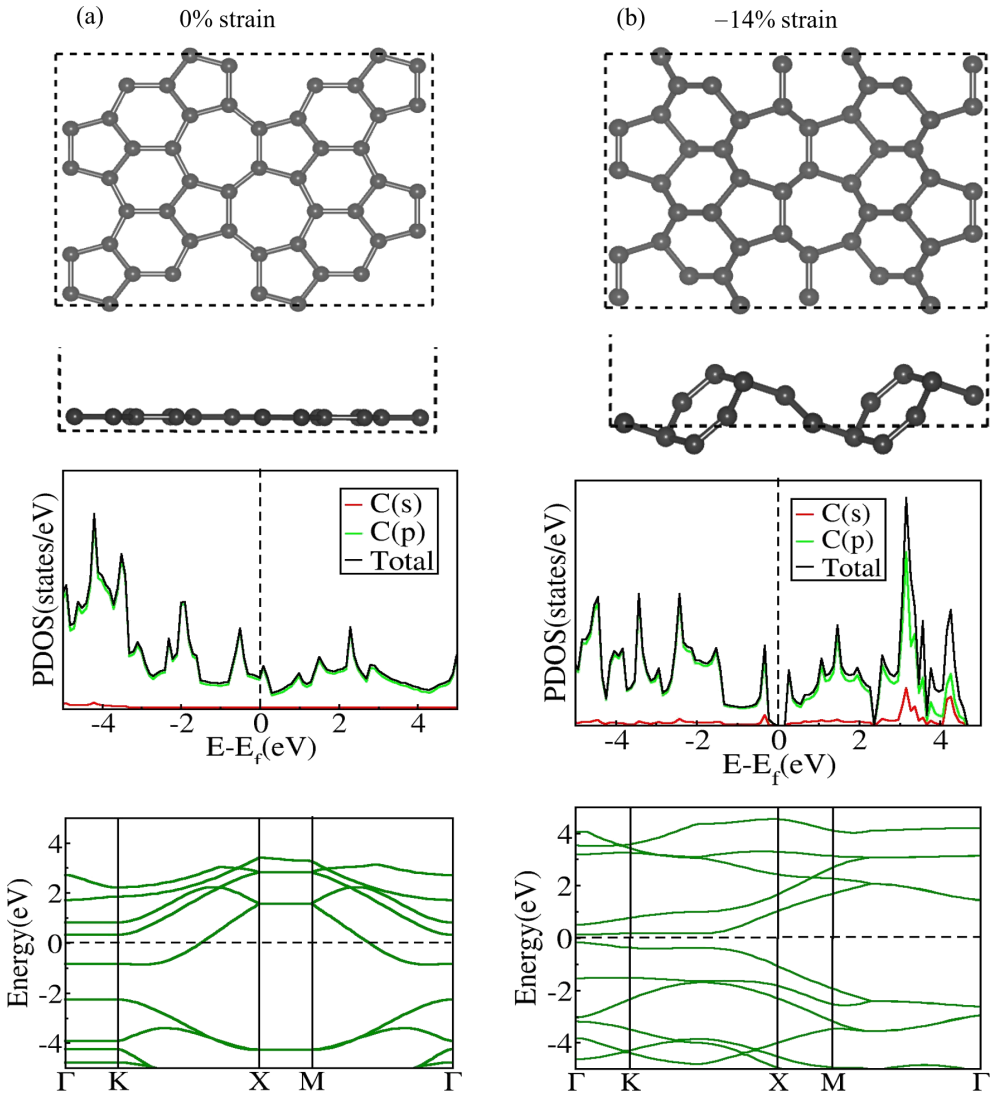

Figure 2: Relaxed 2 × 2 × 1 supercell's top and side views, PDOS, and EBS of ψ-graphene (a) at 0% and (b) −14% strain. A direct-bandgap opening of 0.2 eV was found at −14% strain. We observe a buckling height of 2.13 Å at −14% applied strain.

buckling, and only above this strain value buckling was observed in ψ-graphene sheets, as shown in Table 2 for −13% to −17% strain. Hence, within the negative strain range of −1% to −10%, ψ-graphene maintains its flat structural profile, but buckling appears beyond −10% strain. Notably, at the point of emergence of a bandgap (at −14%), the buckling becomes 2.13 Å (Table 2). Thus, in ψ-graphene, the bandgap remains zero with expansion (positive strain) along the lattice plane, while a negative strain of −14% generates a gap of 0.2 eV between its energy bands.

Structural and electronic properties of ψ-graphone with strain

We tabulate the structural parameters, buckling heights, and electronic bandgap values of all strained structures in Table 3.

Positive strain

As mentioned earlier, like pristine ψ-graphene, partially hydrogenated ψ-graphene, ψ-graphone, is also a zero-bandgap material. Structures, PDOS, and EBS of all strained structures are given in Supporting Information File 1, Figures S6, S7, and S8, respectively. A bandgap opening of 0.5 eV was observed at the modest positive strain value of just +1% (Table 3, Figure 3), indicating that the electronic properties of ψ-graphone can be tuned with minimum structural deformation and low energy consumption. As can be seen from Table 3, the bandgap of ψ-graphone fluctuates with an increase in strain with a maximum bandgap of 2.10 eV at 7% strain. At this level, an elongation of 9.94% is found in d_1 with a buckling height of 1.90 Å as shown in Figure S6 (Supporting Information File 1). Moreover, we also observed a transition from an indirect to a

Table 3: Lattice parameters (a, b), C–C bond lengths (d_1, $d_{C–C}$), average C–C bond length ($d_{C–C(avg)}$), buckling height (h), and bandgap energy (E_g) of ψ-graphone on applying lattice strain.

Applied strain	Lattice parameters (Å)		d (Å)				h (Å)	E_g (eV)	Bandgap type
	a	b	d_1	$d_{C–C}$	$d_{C–C(avg)}$	$d_{C–H}$			
−16%	5.63	4.06	1.47	1.39–1.52	1.46	1.10–1.12	1.88	0.70	indirect
−15%	5.69	4.11	1.48	1.39–1.54	1.46	1.10–1.12	1.84	0.80	indirect
−13%	5.83	4.21	1.50	1.40–1.54	1.47	1.11–1.12	1.81	1.30	indirect
−10%	6.03	4.35	1.53	1.42–1.55	1.48	1.10–1.12	1.52	2.00	indirect
−7%	6.23	4.50	1.57	1.45–1.70	1.58	1.10–1.13	1.90	2.31	direct
−5%	6.36	4.59	1.57	1.44–1.57	1.51	1.10–1.13	1.52	2.31	direct
−3%	6.50	4.69	1.58	1.45–1.57	1.51	1.11–1.14	1.90	1.51	indirect
−2%	6.57	4.74	1.59	1.43–1.57	1.50	1.10–1.15	1.89	1.00	indirect
−1%	6.63	4.01	1.53	1.42–1.57	1.50	1.11–1.13	1.81	1.60	indirect
0%	6.70	4.83	1.61	1.47–1.57	1.52	1.11–1.14	1.79	0.00	–
1%	6.77	4.88	1.62	1.48–1.62	1.55	1.11–1.15	1.03	0.500	indirect
2%	6.83	4.93	1.64	1.43–1.59	1.51	1.11–1.15	0.98	0.300	indirect
3%	6.90	4.98	1.66	1.43–1.60	1.52	1.11–1.15	0.95	1.10	direct
5%	7.03	5.08	1.70	1.41–160	1.51	1.11–1.14	1.02	1.12	indirect
7%	7.17	5.17	1.77	1.37–1.62	1.50	1.10–1.12	1.00	2.10	direct
10%	7.37	5.46	2.17	1.42–1.73	1.58	1.10–1.12	1.02	0.300	direct
13%	7.57	5.46	2.05	1.47–1.78	1.62	1.11–1.12	1.03	2.00	indirect
15%	7.71	5.56	2.80	1.45–1.64	1.64	1.05–1.11	1.36	1.70	direct
16%	7.77	5.61	2.83	1.45–1.94	1.70	1.09–1.11	1.34	1.50	direct

direct bandgap with a change in strain values applied to ψ-graphone sheets. Beyond the +10% strain level, suddenly, the separation between the bands increases to 2.00 eV, and on further increasing the magnitude of applied positive strain, it reduces to 1.50 eV at +16% strain value.

Negative strain

A remarkable observation is made regarding the electrical properties (Supporting Information File 1, Figures S9 and S10) when ψ-graphone undergoes negative mechanical strain ranging from −1% to −16% in its lattice plane. ψ-Graphone maintains its semiconducting nature within this negative strain range, and random separation is found between the valence and conduction bands of electrons, that is, within this negative strain range, the bandgap energies fluctuate for different strain values. The bandgap narrows at certain extents of deformation and widens at others. However, similar to positive strain, even a slight compression of −1%, which denotes a slight reduction in the lattice parameters, was found to be sufficient for a metal-to-semiconductor transition in ψ-graphone (Figure 3). These results indicate the extreme sensitivity of the ψ-graphone crystal structure to mechanical strain (tensile or compressive). As the magnitude of strain increases beyond −1%, the bandgap increases and reaches a stable value of 2.31 eV within a negative strain range of −5% to −7%. However, beyond the −7% strain level, a continuous reduction is observed in the bandgap, which continues up to −16% strain. At this level, the bandgap becomes 0.7 eV, signifying the smallest bandgap value and the limit of applying negative strain on ψ-graphone. Thus, initially, ψ-graphone transitions from a narrow bandgap, proof of its semiconducting behavior, to a wide bandgap. However, on further increasing the negative strain, it exhibits a reversal in its bandgap from a wider gap to a narrower one. Another intriguing observation shown in Table 3 is the nature of the bandgap at various negative strain values. Only in the specific span of −5% to −7%, where the bandgap becomes stable, a direct transition of electrons from the valence to the conduction band is allowed. Outside this strain range, ψ-graphone has an indirect bandgap. Furthermore, the buckling height of ψ-graphone increased from initially 1.79 to 1.90 Å at strain levels of −3% and −7%, signifying its lowest mechanical stability at these strain levels. Although the presence of negative strain affects the lengths of all C–C bonds of ψ-graphone, the bond length d_1 at the junction of the *s*-indacene molecule reaches its minimum value of 1.47 Å at −16% strain along the lattice plane, which indicates that only 8.69% contraction is possible in this specific bond length of ψ-graphone. The bond length between C atoms and attached H atoms typically ranges from 1.05 to 1.15 Å.

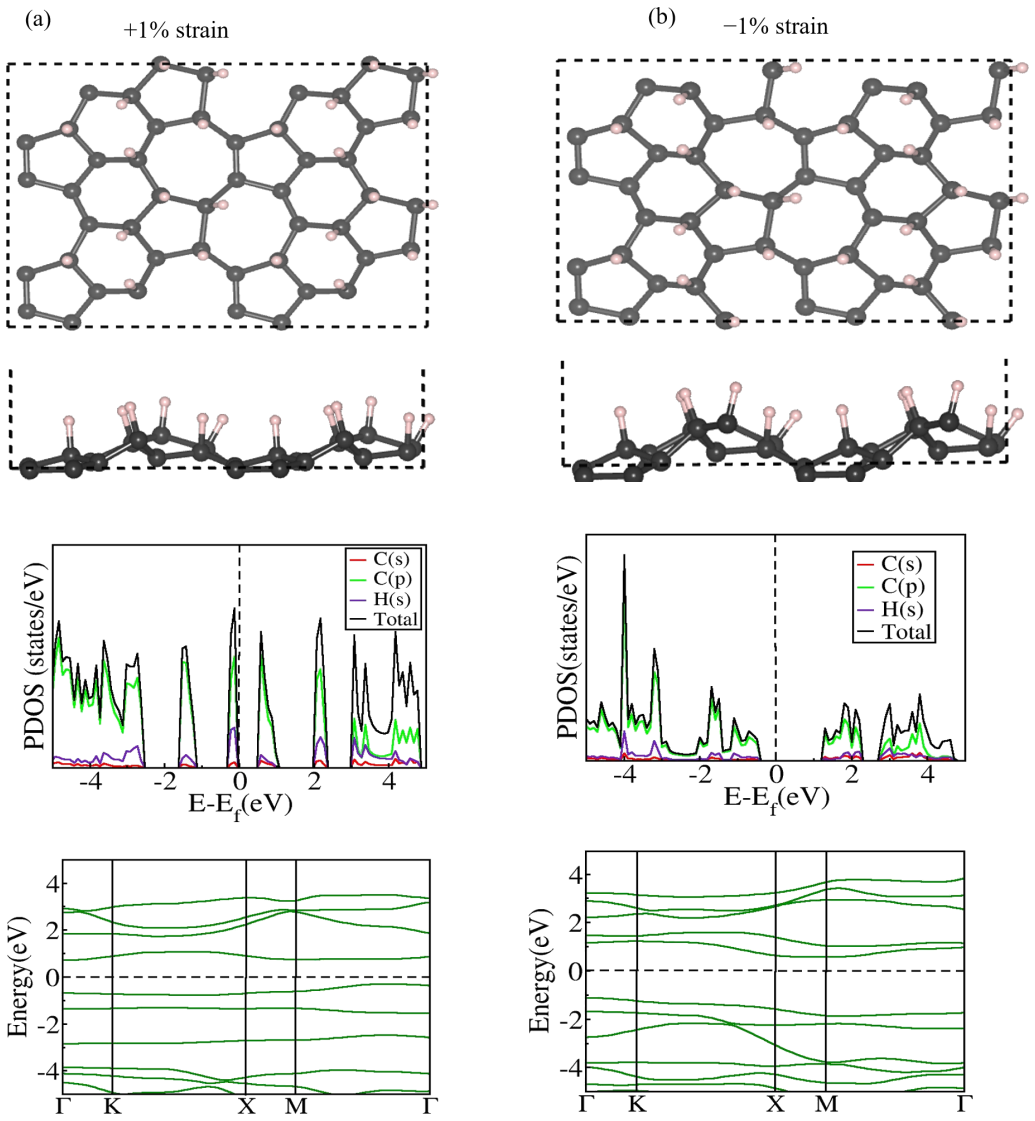

Figure 3: Relaxed 2 × 2 × 1 supercell's top and side views, PDOS, and EBS of ψ-graphone (a) at +1% and (b) at −1% strain values. An opening of indirect bandgaps of 0.5 and 1.6 eV was found at +1% and −1% strain, respectively.

Structural and electronic properties of ψ-graphane with strain

We tabulate the structural parameters, buckling height, and electronic bandgap values of all strained structures in Table 4.

Positive strain

Next, we applied positive mechanical strain to fully hydrogenated ψ-graphene, that is, ψ-graphane (Supporting Information File 1, Figure S11). As mentioned earlier, a bandgap of 3.78 eV is observed in the pristine ψ-graphane sheet. When ψ-graphane undergoes positive strain, the C–C bonds expand freely, leading to an increment in d_1 from 1.56 Å to 1.80 Å at a strain level of +17% as shown in Table 4, where we tabulate structural parameters and bandgap of all strained structures. Unlike ψ-graphone, the mechanical strain does not affect the C–H bond length, which remains fixed at 1.10–1.11 Å, indicating the formation of strong C–H bonds in ψ-graphane compared to ψ-graphone. We note a linear bandgap increase in ψ-graphane from 3.78 to 4.81 eV when the strain is increased from 0 to 17% (Figures S12 and S13, Supporting Information File 1). Furthermore, ψ-graphane exhibits a direct bandgap at all applied strain values, and electrons cannot move from the valence to the conduction band even when strain is applied. This direct bandgap allows the most efficient transport of charge carriers and easy recombination of electrons and holes, indicating its suitability in quantum computing, which requires semiconductors with direct bandgaps. ψ-Graphane can endure up to +17% mechanical strain (Figure 4) suggesting that the

Table 4: Lattice parameters (a, b), C–C bond lengths (d_1, $d_{C–C}$), average C–C bond length ($d_{C–C(avg)}$), buckling height (h), and bandgap energy (E_g) of ψ-graphane on applying lattice strain.

Applied strain	Lattice parameters (Å)		d (Å)				h (Å)	E_g (eV)	Bandgap type
	a	b	d_1	$d_{C–C}$	$d_{C–C(avg)}$	$d_{C–H}$			
−17%	5.56	4.01	1.43	1.33–1.54	1.43	1.10–1.11	2.02	1.40	direct
−16%	5.63	4.06	1.43	1.35–1.53	1.44	1.10–1.11	1.96	1.50	direct
−15%	5.69	4.11	1.42	1.35–1.46	1.41	1.10–1.11	1.98	1.80	direct
−13%	5.83	4.21	1.43	1.36–1.51	1.44	1.10–1.11	1.92	1.90	direct
−10%	6.03	4.35	1.45	1.38–1.50	1.44	1.10–1.11	1.70	2.21	direct
−7%	6.23	4.50	1.48	1.41–1.49	1.45	1.10–1.11	1.42	2.70	direct
−5%	6.36	4.59	1.50	1.44–1.50	1.47	1.10–1.11	1.01	3.00	direct
−3%	6.50	4.69	1.53	1.45–1.51	1.48	1.10–1.11	0.85	3.30	direct
−2%	6.57	4.74	1.54	1.47–1.51	1.49	1.10–1.11	0.97	3.41	direct
−1%	6.63	4.01	1.55	1.49–1.52	1.51	1.10–1.11	0.91	3.61	direct
0%	6.70	4.83	1.56	1.49–1.55	1.52	1.10–1.11	0.85	3.78	direct
1%	6.77	4.88	1.58	1.50–1.54	1.52	1.10–1.11	0.85	3.80	direct
2%	6.83	4.93	1.59	1.51–1.56	1.54	1.10–1.11	0.81	3.90	direct
3%	6.90	4.98	1.61	1.53–1.58	1.56	1.10–1.11	0.78	4.00	direct
5%	7.03	5.08	1.64	1.54–1.63	1.59	1.10–1.11	0.74	4.11	direct
7%	7.17	5.17	1.67	1.56–1.63	1.60	1.10–1.11	0.70	4.31	direct
10%	7.37	5.46	1.76	1.61–1.68	1.65	1.10–1.11	0.65	4.50	direct
13%	7.57	5.46	1.75	1.61–1.72	1.66	1.10–1.11	0.63	4.70	direct
15%	7.71	5.56	1.78	1.62–1.75	1.68	1.10–1.11	0.62	4.70	direct
16%	7.77	5.61	1.79	1.64–1.76	1.70	1.10–1.11	0.61	4.81	direct
17%	7.84	5.66	1.80	1.64–1.78	1.71	1.10–1.11	0.61	4.81	direct

bandgap of ψ-graphane can be increased up to 27.25% by positive mechanical strain. Unlike ψ-graphone, which shows fluctuations in buckling height, the buckling height of fully hydrogenated ψ-graphene consistently decreases on increasing the applied positive strain. It reduces to 0.61 Å at both +16% and +17% strain levels.

Negative strain

The cell parameters of ψ-graphane can be compressed by imposing a negative mechanical strain up to −17% from a = 6.70 Å and b = 4.83 Å to a = 5.56 Å and b = 4.01 Å (Table 4, Supporting Information File 1, Figure S11). ψ-graphane can tolerate a mechanical strain range from −17% to +17% before experiencing structural distortion. Introducing negative mechanical strain to ψ-graphane, akin to the effect of positive mechanical strain, does not result in the disappearance of the electronic bandgap at any strain level. Additionally, despite the presence of negative mechanical strain, the type of bandgap of ψ-graphane remains direct, similar to the positive strain effect in ψ-graphane; however, a continuous reduction in bandgap was observed with an increase in negative strain values. At −17% strain level, the bandgap (Figure 4) and d_1 converge to 1.40 eV and 1.43 Å, respectively (Table 4), while the buckling height increases to 2.02 Å. Neither exposing ψ-graphane to negative strain yielded any discernible alteration in the C–H bond lengths, nor did the application of positive strain. Throughout the range from −17% to +17%, ψ-graphane exhibits the behavior of a wide-bandgap semiconductor (Figures S14 and S15, Supporting Information File 1). The carbon p orbitals provide the major contribution to the valence band. In contrast, in the conduction band, the s orbitals of carbon and hydrogen atoms and the p orbitals of carbon atoms contribute equally.

We have plotted the variation in bandgap and buckling height in ψ-graphene, ψ-graphone, and ψ-graphane 2D sheets in Figure 5. It can be seen easily that in ψ-graphene, the application of negative strain opens up a bandgap of 0.2 eV at −14%, which reaches a maximum value of 0.7 eV at −16% strain with a buckling height of 2.3 Å. Here, positive strain fails to open the bandgap. In ψ-graphone, a fluctuation in the bandgap is observed with a bandgap opening at 1% values of positive and negative strain. In ψ-graphane, the bandgap increases linearly with applied positive strain from its original value of 3.78 to 4.81 eV at 17%, while a linear decrease in bandgap is observed with negative strain.

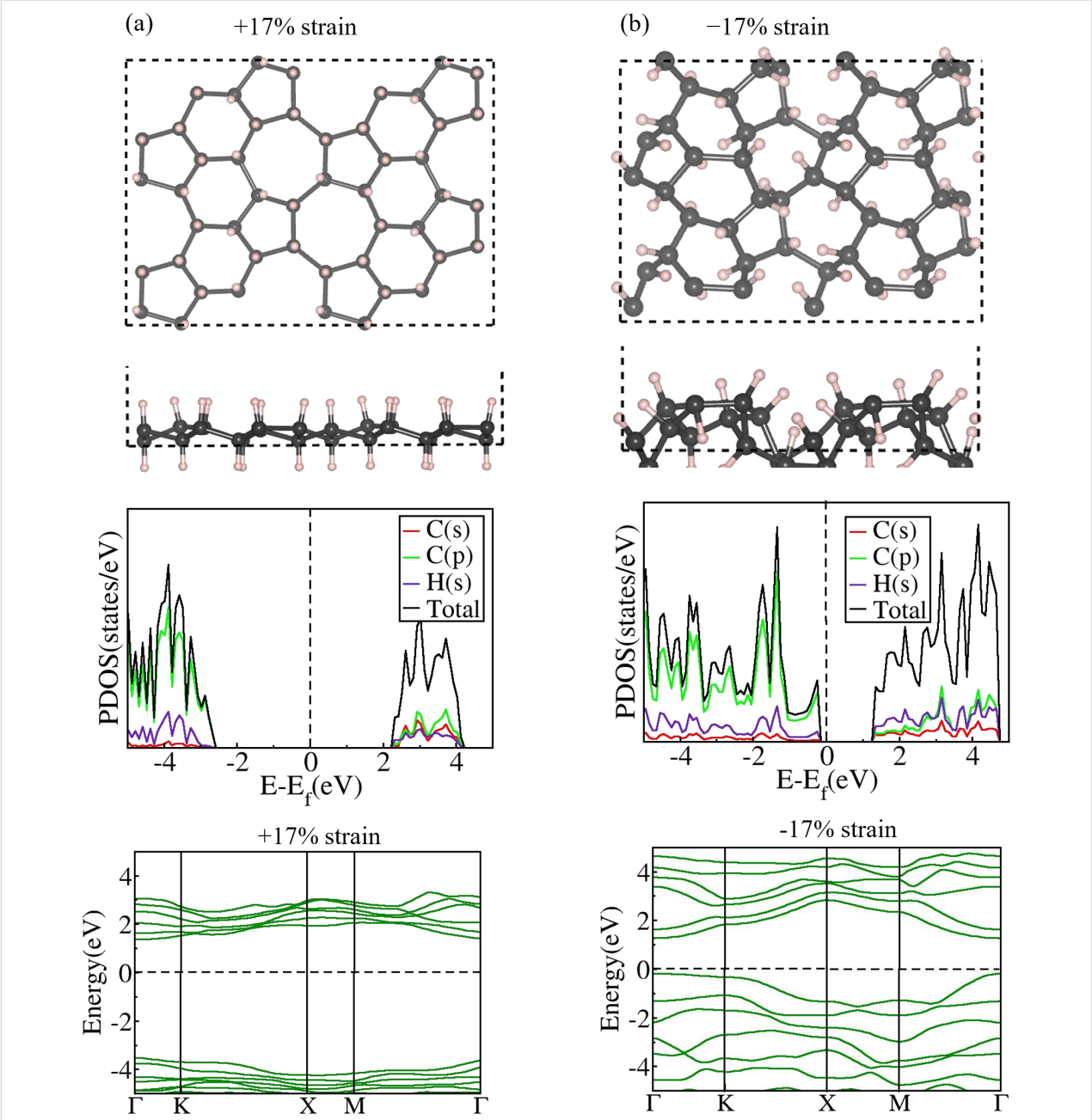

Figure 4: Relaxed 2 × 2 × 1 supercell's top and side views, PDOS, and EBS of ψ-graphane (a) at −17% and (b) +17% strain values. The bandgap of ψ-graphane becomes maximum at +17% strain (4.81 eV) and minimum at −17% (1.40 eV) strain values. The type of the bandgap at both strain levels was observed to be direct.

Conclusion

In this study, we explored the structural and electronic properties of ψ-graphene and its partially and fully hydrogenated forms ψ-graphone and ψ-graphane, respectively, upon introducing mechanical strain. We observed that strain engineering affects the bandgap of pristine and hydrogenated ψ-graphene 2D nanosheets. In summary, positive strain along the lattice plane of ψ-graphene cannot create a gap between its energy bands. However, at a negative mechanical strain of around −14%, a bandgap of 0.2 eV becomes apparent in the band structure of ψ-graphene, changing it from zero-bandgap to a narrow-bandgap semiconductor. These results signify ψ-graphene's low bandgap sensitivity to mechanical strain. Enhanced sensitivity to mechanical strain was observed in ψ-graphone, a zero-bandgap material. We found that the bandgap of ψ-graphone can be opened even under a slight strain of −1% or +1%, highlighting the remarkable sensitivity of ψ-graphone towards mechanical deformation. In contrast, ψ-graphane is a direct-

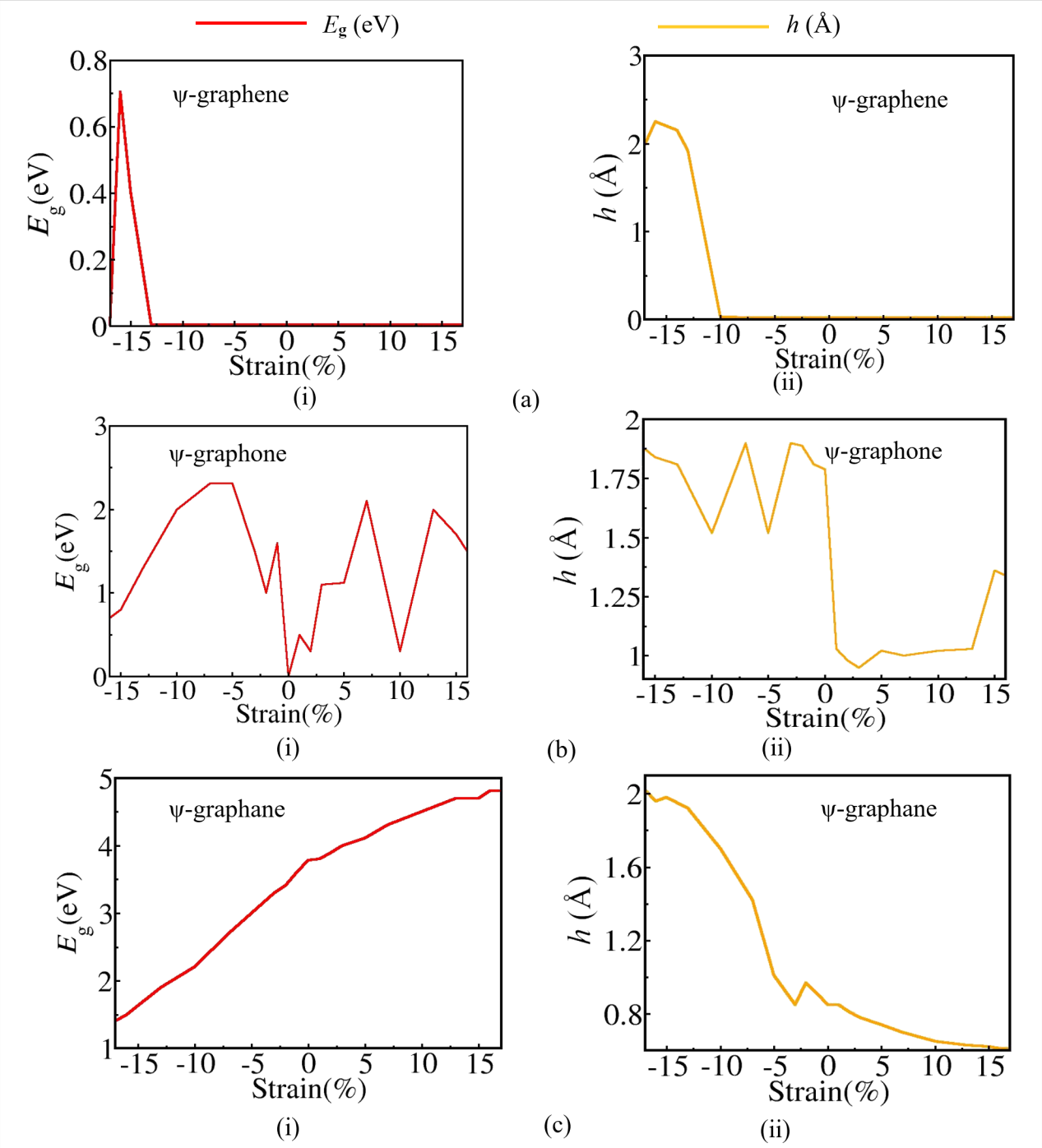

Figure 5: Variation of (i) bandgap energy E_g and (ii) buckling height h of (a) ψ-graphene, (b) ψ-graphone, and (c) ψ-graphane under applied biaxial mechanical strain. The bandgap E_g and buckling height h of ψ-graphane vary in an almost linear fashion.

bandgap material that remains unchanged under mechanical strain. This outcome offers various critical applications of ψ-graphane in photodetectors, solar cells, LEDs, pressure and strain sensors, energy storage, and quantum computing. The mechanical strain tolerance of pristine and fully hydrogenated ψ-graphene is observed to be −17% to +17%, whereas for ψ-graphone, it lies within the strain span of −16% to +16%. The remarkable strain tolerance of these materials makes them promising candidates for flexible displays and other electronic devices.

Computational Methodology

The computational parameters used in our calculations are based on the density functional theory (DFT) as implemented in

Quantum Espresso [46]. Our computations employed the generalized gradient approximation (GGA) and Perdew–Burke–Ernzerhof exchange–correlation functionals [47]. The crystal structure of pristine and hydrogenated ψ-graphene has the space group *P*2*mg* [39]. The unit cell of ψ-graphene contains 12 carbon atoms. In comparison, the unit cells of ψ-graphone and ψ-graphane consist of 12 carbons and six hydrogens and 12 carbons and 12 hydrogen atoms, respectively (Figure 1) [38,39]. For the sampling of the Brillouin zone, we used a well converged 8 × 8 × 1 k-point mesh, and the electronic wave functions were expanded within a basis set of plane waves with a 600 eV cutoff energy. The unwanted interactions between the periodic images of 2D sheets have been mitigated by incorporating a generous vacuum space of 13 Å into our simulation cell. The convergence in self-consistency was achieved at a stringent threshold energy value of 10^{-5} eV, and forces acting on atoms were converged to 0.01 eV.

Supporting Information

We have given relaxed structures, PDOS, and EBS plots of ψ-graphene, ψ-graphone, and ψ-graphane in the Supporting Information. We have also given variations of average bond lengths and d_1 bond lengths with applied uniform biaxial mechanical strain in these three materials.

Supporting Information File 1

Additional figures.
[https://www.beilstein-journals.org/bjnano/content/supplementary/2190-4286-15-116-S1.pdf]

Acknowledgements

Kamal Kumar (KK) and AKM acknowledge the University of Kassel, Germany, for visiting scholar positions and computational resources. Parts of this work have been performed using the Danish National Life Science Supercomputing Centre, Computerome. This work has also used the ARCHER2 UK National Supercomputing Service (https://www.archer2.ac.uk).

Funding

Dr. Abhishek Kumar Mishra (AKM) acknowledges the Science and Engineering Research Board (SERB) for a state university research excellence (SURE) grant (SUR/2022/004935).

Author Contributions

Kamal Kumar: data curation; formal analysis; investigation; methodology; visualization; writing – original draft. Nora H. de Leeuw: resources; software; writing – review & editing. Jost Adam: funding acquisition; project administration; resources; supervision; writing – review & editing. Abhishek Kumar Mishra: conceptualization; data curation; funding acquisition; methodology; project administration; resources; software; supervision; visualization; writing – review & editing.

ORCID® iDs

Kamal Kumar - https://orcid.org/0009-0007-2314-759X
Nora H. de Leeuw - https://orcid.org/0000-0002-8271-0545
Jost Adam - https://orcid.org/0000-0001-7177-3252
Abhishek Kumar Mishra - https://orcid.org/0000-0002-6129-5653

Data Availability Statement

All data that supports the findings of this study is available in the published article and/or the supporting information to this article.

References

1. Geim, A. K.; Novoselov, K. S. *Nat. Mater.* **2007,** *6,* 183–191. doi:10.1038/nmat1849
2. Alemour, B.; Yaacob, M. H.; Lim, H. N.; Roshdi Hassan, M. *Int. J. Nanoelectron. Mater.* **2018,** *11,* 371–398.
3. Velasco, A.; Ryu, Y. K.; Boscá, A.; Ladrón-de-Guevara, A.; Hunt, E.; Zuo, J.; Pedrós, J.; Calle, F.; Martinez, J. *Sustainable Energy Fuels* **2021,** *5,* 1235–1254. doi:10.1039/d0se01849j
4. Jain, V.; Kandasubramanian, B. *J. Mater. Sci.* **2020,** *55,* 1865–1903. doi:10.1007/s10853-019-04150-y
5. Shiraz, H. G.; Tavakoli, O. *Renewable Sustainable Energy Rev.* **2017,** *74,* 104–109. doi:10.1016/j.rser.2017.02.052
6. Podlivaev, A. I.; Openov, L. A. *Semiconductors* **2011,** *45,* 958–961. doi:10.1134/s1063782611070177
7. Sofo, J. O.; Chaudhari, A. S.; Barber, G. D. *Phys. Rev. B: Condens. Matter Mater. Phys.* **2007,** *75,* 153401. doi:10.1103/physrevb.75.153401
8. Zhao, W.; Gebhardt, J.; Späth, F.; Gotterbarm, K.; Gleichweit, C.; Steinrück, H.-P.; Görling, A.; Papp, C. *Chem. – Eur. J.* **2015,** *21,* 3347–3358. doi:10.1002/chem.201404938
9. Elias, D. C.; Nair, R. R.; Mohiuddin, T. M. G.; Morozov, S. V.; Blake, P.; Halsall, M. P.; Ferrari, A. C.; Boukhvalov, D. W.; Katsnelson, M. I.; Geim, A. K.; Novoselov, K. S. *Science* **2009,** *323,* 610–613. doi:10.1126/science.1167130
10. Kashiwaya, S.; Shi, Y.; Lu, J.; Sangiovanni, D.; Andersson, M.; Rosen, J.; Hultman, L. *Res. Square* **2023,** rs–2807259. doi:10.21203/rs.3.rs-2807259/v2
11. Zhu, F.-f.; Chen, W.-j.; Xu, Y.; Gao, C.-l.; Guan, D.-d.; Liu, C.-h.; Qian, D.; Zhang, S.-C.; Jia, J.-f. *Nat. Mater.* **2015,** *14,* 1020–1025. doi:10.1038/nmat4384
12. Yuhara, J.; He, B.; Matsunami, N.; Nakatake, M.; Le Lay, G. *Adv. Mater. (Weinheim, Ger.)* **2019,** *31,* 1901017. doi:10.1002/adma.201901017
13. Wazeer, A. *J. Inst. Eng. (India): Ser. D* **2023,** *104,* 403–412. doi:10.1007/s40033-022-00387-1
14. Kamal, C.; Ezawa, M. *Phys. Rev. B* **2015,** *91,* 085423. doi:10.1103/physrevb.91.085423
15. Yang, L.-M.; Dornfeld, M.; Frauenheim, T.; Ganz, E. *Phys. Chem. Chem. Phys.* **2015,** *17,* 26036–26042. doi:10.1039/c5cp04222d
16. Li, X.; Wang, Q.; Jena, P. *J. Phys. Chem. Lett.* **2017,** *8,* 3234–3241. doi:10.1021/acs.jpclett.7b01364

17. Butler, S. Z.; Hollen, S. M.; Cao, L.; Cui, Y.; Gupta, J. A.; Gutiérrez, H. R.; Heinz, T. F.; Hong, S. S.; Huang, J.; Ismach, A. F.; Johnston-Halperin, E.; Kuno, M.; Plashnitsa, V. V.; Robinson, R. D.; Ruoff, R. S.; Salahuddin, S.; Shan, J.; Shi, L.; Spencer, M. G.; Terrones, M.; Windl, W.; Goldberger, J. E. *ACS Nano* **2013,** *7,* 2898–2926. doi:10.1021/nn400280c
18. Du, J.; Yu, H.; Liu, B.; Hong, M.; Liao, Q.; Zhang, Z.; Zhang, Y. *Small Methods* **2021,** *5,* 2000919. doi:10.1002/smtd.202000919
19. Qi, Y.; Sadi, M. A.; Hu, D.; Zheng, M.; Wu, Z.; Jiang, Y.; Chen, Y. P. *Adv. Mater. (Weinheim, Ger.)* **2023,** *35,* 2205714. doi:10.1002/adma.202205714
20. Xu, X.; Liang, T.; Kong, D.; Wang, B.; Zhi, L. *Mater. Today Nano* **2021,** *14,* 100111. doi:10.1016/j.mtnano.2021.100111
21. Fang, M.; Yang, E.-H. *Materials* **2023,** *16,* 3701. doi:10.3390/ma16103701
22. Peng, Z.; Chen, X.; Fan, Y.; Srolovitz, D. J.; Lei, D. *Light: Sci. Appl.* **2020,** *9,* 190. doi:10.1038/s41377-020-00421-5
23. Yang, S.; Chen, Y.; Jiang, C. *InfoMat* **2021,** *3,* 397–420. doi:10.1002/inf2.12177
24. Liu, F.; Fan, Z. *Chem. Soc. Rev.* **2023,** *52,* 1723–1772. doi:10.1039/d2cs00931e
25. Kim, J. M.; Haque, M. F.; Hsieh, E. Y.; Nahid, S. M.; Zarin, I.; Jeong, K.-Y.; So, J.-P.; Park, H.-G.; Nam, S. *Adv. Mater. (Weinheim, Ger.)* **2023,** *35,* 2107362. doi:10.1002/adma.202107362
26. Hildebrand, M.; Abualnaja, F.; Makwana, Z.; Harrison, N. M. *J. Phys. Chem. C* **2019,** *123,* 4475–4482. doi:10.1021/acs.jpcc.8b09894
27. Manzoor, M.; Kumar, K.; Mishra, A. K.; Al-Asbahi, B. A.; Sharma, R. *Solid State Commun.* **2024,** *386,* 115527. doi:10.1016/j.ssc.2024.115527
28. Roldán, R.; Castellanos-Gomez, A.; Cappelluti, E.; Guinea, F. *J. Phys.: Condens. Matter* **2015,** *27,* 313201. doi:10.1088/0953-8984/27/31/313201
29. Si, C.; Sun, Z.; Liu, F. *Nanoscale* **2016,** *8,* 3207–3217. doi:10.1039/c5nr07755a
30. Ni, Z. H.; Yu, T.; Lu, Y. H.; Wang, Y. Y.; Feng, Y. P.; Shen, Z. X. *ACS Nano* **2008,** *2,* 2301–2305. doi:10.1021/nn800459e
31. Conley, H. J.; Wang, B.; Ziegler, J. I.; Haglund, R. F., Jr.; Pantelides, S. T.; Bolotin, K. I. *Nano Lett.* **2013,** *13,* 3626–3630. doi:10.1021/nl4014748
32. Gui, G.; Li, J.; Zhong, J. *Phys. Rev. B: Condens. Matter Mater. Phys.* **2008,** *78,* 075435. doi:10.1103/physrevb.78.075435
33. Kerszberg, N.; Suryanarayana, P. *RSC Adv.* **2015,** *5,* 43810–43814. doi:10.1039/c5ra03422a
34. Mohan, B.; Kumar, A.; Ahluwalia, P. K. *Phys. E (Amsterdam, Neth.)* **2014,** *61,* 40–47. doi:10.1016/j.physe.2014.03.013
35. Jamwal, P.; Kumar, S.; Muruganathan, M.; Kumar, R. *Surf. Interfaces* **2023,** *41,* 103294. doi:10.1016/j.surfin.2023.103294
36. Cao, H.; Yu, Z.; Lu, P. *Superlattices Microstruct.* **2015,** *86,* 501–507. doi:10.1016/j.spmi.2015.08.006
37. Xu, W.; Lu, P.; Wu, L.; Yang, C.; Song, Y.; Guan, P.; Han, L.; Wang, S. *IEEE J. Sel. Top. Quantum Electron.* **2017,** *23,* 214–218. doi:10.1109/jstqe.2016.2593106
38. Jalilvand, S.; Mousavi, H.; Irani, M. *Mater. Today Commun.* **2022,** *33,* 104833. doi:10.1016/j.mtcomm.2022.104833
39. Faghihnasiri, M.; Mousavi, S. H.; Shayeganfar, F.; Ahmadi, A.; Beheshtian, J. *RSC Adv.* **2020,** *10,* 26197–26211. doi:10.1039/d0ra03104f
40. Khatir, N. M.; Ahmadi, A.; Taghizade, N.; Motevali khameneh, S.; Faghihnasiri, M. *Superlattices Microstruct.* **2020,** *145,* 106603. doi:10.1016/j.spmi.2020.106603
41. Huang, X.; Ma, M.; Cheng, L.; Liu, L. *Phys. E (Amsterdam, Neth.)* **2020,** *115,* 113701. doi:10.1016/j.physe.2019.113701
42. Chakraborty, B.; Vaidyanathan, A.; Kandasamy, M.; Wagh, V.; Sahu, S. *J. Appl. Phys.* **2022,** *132,* 065002. doi:10.1063/5.0098522
43. Kumar, K.; de Leeuw, N.; Adam, J.; Kumar Mishra, A. *ChemRxiv* **2024**. doi:10.26434/chemrxiv-2024-ztx08
44. Chakraborty, B.; Ray, P.; Garg, N.; Banerjee, S. *Int. J. Hydrogen Energy* **2021,** *46,* 4154–4167. doi:10.1016/j.ijhydene.2020.10.161
45. Nair, H. T.; Jha, P. K.; Chakraborty, B. *Int. J. Hydrogen Energy* **2023,** *48,* 37860–37871. doi:10.1016/j.ijhydene.2022.08.084
46. Giannozzi, P.; Andreussi, O.; Brumme, T.; Bunau, O.; Buongiorno Nardelli, M.; Calandra, M.; Car, R.; Cavazzoni, C.; Ceresoli, D.; Cococcioni, M.; Colonna, N.; Carnimeo, I.; Dal Corso, A.; de Gironcoli, S.; Delugas, P.; DiStasio, R. A., Jr.; Ferretti, A.; Floris, A.; Fratesi, G.; Fugallo, G.; Gebauer, R.; Gerstmann, U.; Giustino, F.; Gorni, T.; Jia, J.; Kawamura, M.; Ko, H.-Y.; Kokalj, A.; Küçükbenli, E.; Lazzeri, M.; Marsili, M.; Marzari, N.; Mauri, F.; Nguyen, N. L.; Nguyen, H.-V.; Otero-de-la-Roza, A.; Paulatto, L.; Poncé, S.; Rocca, D.; Sabatini, R.; Santra, B.; Schlipf, M.; Seitsonen, A. P.; Smogunov, A.; Timrov, I.; Thonhauser, T.; Umari, P.; Vast, N.; Wu, X.; Baroni, S. *J. Phys.: Condens. Matter* **2017,** *29,* 465901. doi:10.1088/1361-648x/aa8f79
47. Madsen, G. K. H. *Phys. Rev. B: Condens. Matter Mater. Phys.* **2007,** *75,* 195108. doi:10.1103/physrevb.75.195108

License and Terms